

An Orbit Fit for the Grillmair Dionatos Cold Stellar Stream

Benjamin A. Willett,¹ Heidi Jo Newberg,¹ Haotong Zhang,² Brian Yanny,³ Timothy C. Beers⁴

ABSTRACT

We use velocity and metallicity information from SDSS and SEGUE stellar spectroscopy to fit an orbit to the narrow 63° stellar stream of Grillmair and Dionatos. The stars in the stream have a retrograde orbit with eccentricity $e = 0.33$ (perigalacticon of 14.4 kpc and apogalacticon of 28.7 kpc) and inclination approximately $i \sim 35^\circ$. In the region of the orbit which is detected, it has a distance of about 7 to 11 kpc from the Sun. Assuming a standard disk plus bulge and logarithmic halo potential for the Milky Way stars plus dark matter, the stream stars are moving with a large space velocity of approximately 276 km s^{-1} at perigalacticon. Using this stream alone, we are unable to determine if the dark matter halo is oblate or prolate. The metallicity of the stream is $[\text{Fe}/\text{H}] = -2.1 \pm 0.1$. Observed proper motions for individual stream members above the main sequence turnoff are consistent with the derived orbit. None of the known globular clusters in the Milky Way have positions, radial velocities, and metallicities that are consistent with being the progenitor of the GD-1 stream.

1. Introduction

Data from tidal stream debris is a valuable resource for constraining Galactic structure. In the last decade, several streams, with both globular cluster and dwarf galaxy progenitors, have been discovered in the Milky Way (Ibata et al. 1995; Leon et al. 2000; Yanny et al. 2000; Vivas et al. 2001; Newberg et al. 2002; Martinez-Delgado et al. 2001;

¹Dept. of Physics, Applied Physics, and Astronomy, Rensselaer Polytechnic Institute, Troy, NY 12180; willeb@rpi.edu

²National Astronomical Observatory, Beijing, China;

³Fermi National Accelerator Laboratory, Batavia, IL 60510;

⁴Dept. of Physics and Astronomy, CSCE: Center for the Study of Cosmic Evolution, and JINA: Joint Institute for Nuclear Astrophysics, Michigan State University, E. Lansing, MI 48824, USA; beers@pa.msu.edu

Odenkirchen et al. 2001; Majewski et al. 2003; Grillmair & Johnson 2006; Duffau et al. 2006; Grillmair and Dionatos 2006; Grillmair 2006; Belokurov et al. 2007; Grillmair 2009), as well as in nearby galaxies (Ibata et al. 2001a; Ferguson et al. 2005; Chapman et al. 2008; Martinez-Delgado et al. 2008a,b). By examining the density, kinematics, distribution, and structure of various tidal streams surrounding the Milky Way, a clearer picture of how our halo was built can be developed (Bullock and Johnston 2005). In addition, stellar streams can be used as probes of the Galactic gravitational potential, and thus constrains the shape of the dark matter halo (Ibata et al. 2001b; Helmi 2004; Fellhauer et al. 2006).

Grillmair and Dionatos (2006), hereafter GD, announced the detection of a 63° cold stellar stream in the Galactic halo (the stream itself we refer to henceforth as GD-1, following GD), using stellar density counts extracted from the Sloan Digital Sky Survey (SDSS; York et al. 2000). This stream is extremely narrow, less than 0.25° degrees in width, which is less than 50 pc at their measured distances of 7.3 to 9.1 kpc from the Sun. GD therefore concluded that the progenitor was a globular cluster, but the progenitor remains unidentified and could be completely disrupted.

In this work, we utilize newly available Sloan Extension for Galactic Understanding and Exploration (SEGUE; see Yanny et al. 2009) spectroscopy of stars identified along the stream, that are available in the Sloan Digital Sky Survey (SDSS) Data Release 7 (DR7), to constrain the orbit of the stream and search for possible progenitors.

2. Data Selection

The SDSS imaging survey (Gunn et al. 1998, 2006) has made it possible to detect faint Milky Way halo streams from the spatial distribution of stars because it provides very accurate multicolor photometry for millions of Galactic stars. Even with the well-calibrated SDSS photometry (Fukugita et al. 1996; Smith et al. 2002; Tucker et al. 2006; Hogg et al. 2001; Pier et al. 2003), GD separated the faint structure from the background of Milky Way halo and disk stars only with careful filtering and smoothing techniques (Odenkirchen et al. 2001; Rockosi 2002). To characterize the stream in more detail and to compute an orbit, we reanalyze the imaging data, supplemented through DR7, and then add to it all newly available spectroscopic observations of GD-1 stream stars available in SDSS DR7.

2.1. Imaging

Using the analysis of GD as a guide, stars were selected from the SDSS DR7 (Abazajian et al. 2009) footprint from a rough color-magnitude box restricted to blue F turnoff and upper main sequence stars at distances of 7 to 20 kpc from the Sun (taking into account that the turnoff spans more than a magnitude of absolute magnitudes): $0 < (g - r)_0 < 0.5$, $18 < g_0 < 22$. Magnitudes with 0 subscript indicate those which have been corrected for reddening using the Schlegel, Finkbeiner, & Davis (1998) maps as implemented in SDSS (DR7). All SDSS stars in the DR7 North Galactic cap footprint which are in this color-magnitude box were selected and plotted in an (α, δ) stellar density diagram with pixels 0.5° on a side. Examination of this diagram by eye showed that GD-1 stream stood out weakly from the background, with enough contrast so that the location of several fiducial points along the stream in (α, δ) could be mapped. Low-order polynomials were then fit to the positions of these points. The lowest order best fit was of third order:

$$\delta = -864.5161 + 13.22518\alpha - 0.06325544\alpha^2 + 0.0001009792\alpha^3. \quad (1)$$

By comparison with likely identified spectroscopic stream members we later verified that this polynomial matches the stream position within about 0.6° for $130^\circ < \alpha < 175^\circ$, and within about 1.0° for $120^\circ < \alpha < 130^\circ$ and $175^\circ < \alpha < 220^\circ$.

Next, 147,537 stars within $\pm 0.5^\circ$ of this polynomial fit (a conservative width is used to increase the signal to noise, it is not necessary to identify every star) were selected from $135^\circ < \alpha < 200^\circ$. They represent the ‘on-stream’ data set. For a control sample (‘off-stream’), 158,147 stars were selected within ± 0.5 degrees of a curve offset by 5 degrees in δ from the ‘on-stream’ data over a similar α range. A Hess diagram in $((g - r)_0, g_0)$ of the difference between the on and off stream data (Newberg et al. 2002) was generated and the results are shown in Figure 1.

Figure 1 shows a clear faint turnoff around $((g - r)_0, g_0) \sim (0.25, 19)$ and upper main sequence descending to $g_0 \sim 22.5$. Other features in Figure 1 include an imperfectly subtracted thick disk residual at $(g - r)_0 \sim 0.45$ from $14 < g_0 < 17.5$ and a residual from nearby M dwarfs at $(g - r)_0 \sim 1.4$ and $19 < g_0 < 23$. The stars below the turnoff are concentrated in a relatively narrow band of color and magnitude, as expected for a stream localized in distance from the Sun. Since the stream varies in distance from 7 to about 10 kpc for the stars in this figure, the actual width of the main sequence is substantially narrower than demonstrated here. The blue turnoff of $(g - r)_0 \sim 0.25$ suggests a lower metallicity or younger age than that of the spheroid, which has a turnoff of $(g - r)_0 \sim 0.3$ and $[\text{Fe}/\text{H}] \sim -1.6$. We superimpose with black dots in Figure 1 a fiducial sequence from the cluster M92. The M92 sequence was calculated by starting with the fiducial sequence in underreddened $r, (g - r)$

from An et al. (2008), converting it to $M_{g_0}, (g - r)_0$ using $E(B-V)$ of 0.02 and a distance to M92 of 8.2 kpc, as tabulated by Harris (1996), and then shifting it to the approximate distance to the GD-1 stream, which is approximately 9 kpc over this range of RA (distance modulus $m - M = 14.76$). This low-metallicity cluster, with $[Fe/H] = -2.3$ (Harris 1996), fits the main sequence and the turnoff reasonably well. We do not see the giant branch or the horizontal branch (which should be at $g_0 \sim 15.5$) in this figure, but given the faintness of the stream that is not unexpected.

We now refine the rough color-magnitude box used to detect the stream in equatorial coordinates. The refined box is selected to allow for a stream which changes distance by $\sim 30\%$ over $90^\circ < \alpha < 260^\circ$. The box is defined as the union of three selection regions heavily outlined in Figure 1: A) $0.15 < (g - r)_0 < 0.31, 17.75 < g_0 < 19.7$ (turn off) B) $0.15 < (g - r)_0 < 0.4, 19.7 \leq g_0 < 20.5$ (lower turn off) and C) $20.5 < g_0 < 22, 17.89 < g_0 - 6.52(g - r)_0 < 19.52$ (upper main sequence). All stars with images in the SDSS DR7 Northern Galactic Cap region which meet these criteria (and have $(u - g)_0 > 0.4$ to exclude quasars), are selected and plotted in (α, δ) in the upper panel of Figure 2. The GD-1 stream is faintly visible, running in an arc from about $(\alpha, \delta) = (220^\circ, 58^\circ)$ through $(164^\circ, 48^\circ)$, then down to $(139^\circ, 22^\circ)$ where it crosses in front of the Sagittarius stream, and then it is not clearly visible as it is lost in Monoceros and other Galactic halo stars near $(126^\circ, 0^\circ)$. The lower panel of Figure 2 presents the same data in a Galactic polar projection. The GD-1 stream is clearly visible. There are several features in the density of stars along the stream of unknown origin. They could be the remains of a nearly dissolved progenitor, the result of interactions between the stream and the potential of the Milky Way's disk and halo, or unassociated spheroid substructure.

The kinematics of the stream, detailed below, reveal that it is on a retrograde orbit moving through the sequence of points in the order just described for the upper panel of Figure 2. Numerous other dwarf galaxies, streams and halo overdensities are present in Figure 2; these will not be discussed further here.

2.2. Spectroscopy

The SEGUE survey (Yanny et al. 2009), which is one of three surveys carried out as part of SDSS-II, obtained spectra of approximately 240,000 Milky Way stars toward ~ 200 sightlines that each covered seven square degrees of the sky, with an emphasis on obtaining spectra of fainter halo stars. While most of SEGUE's 200 observing tiles were randomly distributed across the SDSS imaging footprint, a few were placed on streams of known interest, including the GD-1 stream.

All SEGUE spectra were processed through the standard SDSS spectroscopic reduction pipelines (Stoughton et al. 2002), from which radial velocities accurate to about 10 km s^{-1} for objects at $g \sim 19.5$ were determined. In addition, the stellar spectra were processed through the SEGUE stellar parameter pipeline (SSPP) (Lee et al. 2008a,b; Allende Prieto et al. 2008) in order to obtain abundance ($[\text{Fe}/\text{H}]$), surface gravity ($\log g$), and other atmospheric parameter estimates.

We select from the SDSS-II/SEGUE DR7 database all measured parameters of the 12,825 spectra of stars within 1.3° of the GD-1 stream described by Eq. 1. We further refined the selection to exclude objects far away from the fiducial M92 curve of Figure 1 by requiring that they meet these color magnitude cuts: $-0.3 < (g-r)_0 < 0.15$, $14 < g_0 < 17.75$ or $0.15 < (g-r)_0 < 0.4$, $17.75 < g_0 < 20.5$ or $0.4 < (g-r)_0 < 0.5$, $15.31 < g_0 < 19.14$ or $0.5 < (g-r)_0 < 0.59$, $14 < g_0 < 19.14$ or $0.59 < (g-r)_0 < 0.77$, $14 < g_0 < 17.21$ or $0.77 < (g-r)_0 < 1.2$, $14 < g_0 < 15.31$. The region bounded by these cuts is outlined with a light line in Figure 1. Most of the 4568 remaining spectra are concentrated in 3° diameter patches centered on SEGUE tiles, but some are part of the SDSS-I and SDSS-II Legacy surveys. These latter surveys targeted nearly the entire SDSS footprint spectroscopically, but with few and limited signal-to-noise on stellar targets (since the SDSS Legacy survey primarily targets galaxy and quasar candidates).

We show in Figure 3 the line-of-sight, Galactic standard of rest velocities, v_{gsr} , for each star in the sample, as a function of Galactic longitude. We calculate v_{gsr} using: $v_{\text{gsr}} = \text{RV} + 10.1 \cos b \cos l + 224 \cos b \sin l + 6.7 \sin b$, where RV is the heliocentric radial velocity in km s^{-1} and (l, b) are the standard, Sun-centered Galactic coordinates of each star. A sine curve with amplitude 110 km s^{-1} traces an approximate locus of nearby disk stars co-rotating with the Sun. Spheroid stars occupy a broad range of v_{gsr} centered at $v_{\text{gsr}} = 0$. Seven regions of interest are marked along the bottom of Figure 3, indicating areas with SEGUE plates, where stars identified with the GD-1 stream will be selected. The positions of these seven regions on the sky in equatorial coordinates are also indicated with circles and numbered in the upper panel of Figure 2. Regions 5 and 6 were specially targeted by SEGUE with a tile directly on locations along the GD-1 stream.

From examination of Figure 3, it appears that there is an excess of stars off the rotating disk locus at $v_{\text{gsr}} \sim -90 \text{ km s}^{-1}$ in regions 5 and 6. To confirm that these are in fact GD-1 stream stars, we isolate the stars in regions 5 and 6 and plot their velocity histogram in Figure 4.

The distribution in Figure 4 is overlaid with Gaussians for the thick disk (dispersion of 30 km s^{-1} and an offset of $\mu \sim 20 \text{ km s}^{-1}$), and inner halo (dispersion of 100 km s^{-1}). A significant peak is detected at $v_{\text{gsr}} \sim -82 \text{ km s}^{-1}$ which we associate with the GD-1 stream

member stars.

We next examine the metallicity distribution of stars in this velocity peak in order to estimate the elemental abundance of the GD-1 stream. Later in the paper we will show that the individual v_{gsr} velocities in regions 5 and 6 are 71 ± 2 and 87 ± 2 km s⁻¹, respectively, so we chose a “peak” velocity range of $-97 < v_{gsr} < -61$ km s⁻¹.

Figure 5 shows the SSPP abundance estimates for all stars with good metallicity estimates (for a good estimate a turnoff star generally needs to be brighter than about $g \sim 19$). Errors on individual stars [Fe/H] are approximately 0.3 dex for spectral type F objects with $g < 18.5$. The histogram for all abundances of stars in regions 5 and 6 are plotted with a light line (1311 stars), those for stars in the velocity peak of Figure 4 are indicated with a heavy line (115 stars). The stars with velocities of the GD-1 stream are heavily biased towards lower metallicity stars, compared with those of the thick disk ([Fe/H] ~ -0.7), or inner halo ([Fe/H] ~ -1.6).

We estimate from Figure 4 that about 30 stars in the spectroscopic dataset are from the GD-1 stream. To see the metallicity distribution of the stars in the GD-1 stream, we subtract a scaled version of the histogram with the light line from the histogram with the heavy line. The scaling factor is $(115-30)/(1311-30)$. Since the stars in the velocity selected region contain a smaller fraction of thick disk stars, the subtracted histogram is oversubtracted at high metallicities, and likely undersubtracted at spheroid metallicities. The mean of the stars in the shaded region is [Fe/H]=-1.9, but the real metallicity of the stream is probably somewhat lower than this. Bins with negative counts do not appear in Figure 5.

We now return to the sample of stars in Figure 3, and select only those of very low metallicity ($-2.3 < [\text{Fe}/\text{H}] < -1.65$) in order to isolate stream members from the thick disk and halo field star populations. The low metallicity spectra with positions, colors, and magnitudes that make them candidates for GD-1 stream members are shown in Figure 6. Several velocity peaks are now clearly separated from the disk and spheroid. We now examine stars in each of the seven regions numbered in Figure 6 and determine their observational properties.

3. Photometric Distance estimation

We estimated the distance to the GD-1 stream at the positions of each of the seven regions that it overlaps using a matched filter algorithm. We first generated the Hess diagram from SDSS DR7 data from a region about 5° wide in RA and 1° wide in Dec in the vicinity of each plate, centered on the polynomial fit to the GD-1 stream. Then the Hess diagram of the

background was generated from two regions of sky with the same angular extent on the sky, but offset 1.5° higher and 1.5° lower in declination. The background Hess diagram (divided by two to correct for the difference in sky area) was subtracted from the corresponding Hess diagram on the GD-1 stream. The subtracted Hess diagrams are shown in Figure 7.

Since the GD-1 stream is of quite low metallicity, we selected the globular cluster M92 ($[\text{Fe}/\text{H}] \sim -2.3$) to compare with the observations. We then constructed a M92 filter Hess diagram with the similar method to Grillmair (2009). We first broaden the M92 fiducial sequence from An et al. (2008) with the SDSS photometric errors. Because we do not have a luminosity function for M92 stars, we used the luminosity function of M13, estimated from SDSS survey counts vs. magnitude for stars away from the core of M13, to create the Hess diagram. As before, we assume the distance to M92 is 8.2 kpc.

The M92 filter was shifted from -0.5 to 1.5 magnitudes in r in steps of 0.05 mag. For each shift, we cross-correlated the M92 filter with the subtracted Hess diagram:

$$a(\delta r) = \sum_{g-r,r} [O(g-r,r) - B(g-r,r)] \cdot F(g-r,r+\delta r) \quad (2)$$

and estimated the error of cross-correlation function as:

$$\sigma(a) = \left\{ \sum_{g-r,r} [O(g-r,r) + B(g-r,r)] \cdot F^2(g-r,r+\delta r) \right\}^{0.5}. \quad (3)$$

In the above equations, O and B represent the Hess diagrams of orbit and background segments, respectively. F is the value of M92 filter.

Then we define the maximum position, δr_m , of the cross-correlation function to be the actual distance modulus to the stream. Near the maximum, we can estimate the cross-correlation function by the Taylor expansion:

$$a(\delta r) = a(\delta r_m) + \left. \left(\frac{da}{d\delta r} \right) \right|_{\delta r=\delta r_m} \delta r + \frac{1}{2} \left. \left(\frac{d^2a}{d\delta r^2} \right) \right|_{\delta r=\delta r_m} \delta r^2 + \dots \quad (4)$$

The second term in the right equals zero, since the first derivative is zero at maximum. We use the above Taylor expansion, using only the lowest order non-zero terms, to estimate the error in the cross-correlation function:

$$\sigma^2(a) = \langle a^2(\delta r) - a^2(\delta r_m) \rangle = a(\delta r_m) \left. \left(\frac{d^2a}{d\delta r^2} \right) \right|_{\delta r=\delta r_m} \langle \delta r \rangle^2. \quad (5)$$

Since $\langle \delta r \rangle = \sigma_{\delta r}$,

$$\sigma_{\delta r} = \sqrt{\frac{\sigma^2(a)}{a(\delta r_m) \left. \frac{d^2a}{d\delta r^2} \right|_{\delta r=\delta r_m}}} \quad (6)$$

The distance and corresponding error of each of the seven points along the stream with SEGUE spectra are listed in Table 1. Figure 8 shows the same data as Figure 7, but overplotted with the M92 fiducial sequence shifted to the best estimated distance for each sky position.

4. Notes on Individual Regions

Figure 9 shows velocity histograms of low metallicity stars from Figure 6 within $\pm 1.3^\circ$ of each selected region. A Gaussian velocity histogram, representing a halo distribution with $\sigma = 100 \text{ km s}^{-1}$ and are normalized so that the area under the curve equals the number of stars in the histogram, is also shown. The region number is indicated in the upper right corner of each panel, and the velocity of the peak most likely associated with the GD-1 stream is also indicated. We list below some details of each region’s selection, including the SDSS/SEGUE plates on which most of the objects were detected.

In each region with a clear stream detection, the velocity and velocity dispersion for the GD-1 stream were computed using an iterative method that used only stars within one standard deviation of the mean velocity. We computed the mean and standard deviation of the stars near the velocity peak. Then, we selected stars that were within one standard deviation of the mean and re-computed the mean and standard deviation. The standard deviation calculated this way is an underestimate, since we have removed the tails of the distribution. We corrected the standard deviation assuming Gaussian tails. This process was repeated until the computed mean and standard deviation matched the mean and standard deviation used to select the stars in the stream.

Table 2 lists 48 high confidence GD-1 stream members. The sample includes the stars in Figure 6 (which are selected based on angular distance from the GD-1 stream, photometric color and magnitude, and metallicity) which have Galactic longitude within two degrees of the seven plate centers, have velocities near the measured or expected velocities for the GD-1 stream, and which have proper motions that are consistent with our GD-1 stream model (presented in §7). The velocity cuts for each of the seven regions are: 1) $97 < v_{gsr} < 118$, 2) $59 < v_{gsr} < 79$, 3) $32 < v_{gsr} < 52$, 4) $-17 < v_{gsr} < 3$, 5) $-78 < v_{gsr} < -58$, 6) $-97 < v_{gsr} < -77$, and 7) $-166 < v_{gsr} < -146$. The proper motions expected for each of the seven regions are listed in Table 1. The stars in Table 2 are within two sigma of the expected proper motions, where one sigma is 3 mas/yr in each of μ_l and μ_b . Table 2 includes each objects SDSS-ID number, coordinates, magnitude, colors, velocity, estimated metallicity, surface gravity and proper motion. The proper motions (μ_l , μ_b) listed here are from the USNO-B/SDSS catalog of Munn et al. (2004), as extracted from the DR7

database’s ‘propermotions’ table. Errors on an individual $g \sim 18$ star’s measurement are about 3 mas yr^{-1} on each coordinate.

4.1. Primary Kinematic Regions

Regions 4, 5, and 6 were specifically targeted by SEGUE with plates along the GD-1 stream. These regions, along with region 1, targeted by the SDSS Legacy survey, constitute the 4 regions along the stream with spectroscopy used to fit a model orbit for GD-1.

Region 4, Plates 2889 and 2914: The GD-1 stars are well sampled in this plate pair; there is a clearly detected peak of (primarily) F turnoff stars at $v_{gsr} = -7 \pm 1 \text{ km s}^{-1}$ with $\sigma = 3.9 \text{ km s}^{-1}$, in the magnitude range $17.5 < g_0 < 19.5$. The metallicity of stars in the velocity peak is about $[\text{Fe}/\text{H}] \sim -2.2$. There are two BHBs in this sample near $g \sim 14.9$, corresponding to a distance of 7.2 kpc (Sirko et al. 2004). The distance to this region derived in Section 3 from the turnoff photometry is $7.5 \pm 0.33 \text{ kpc}$, in good agreement with the BHB magnitudes. The velocities of the two BHBs are -6 and -3 km s^{-1} , in excellent agreement with the average of the turnoff star velocities, as are the metallicities ($[\text{Fe}/\text{H}] = -2.0$ and -2.1 , respectively).

Region 5, Plates 2557 and 2567: The plate spans the full width of the GD-1 stream. There is a strong peak in the velocity distribution. This peak has $v_{gsr} = -71 \pm 2 \text{ km s}^{-1}$ with $\sigma = 5.3 \text{ km s}^{-1}$. The average g magnitude in this range is $g \sim 19$, which is consistent with the distance estimation from color magnitude turnoff fitting. The metallicity distribution of F turn-off stars in the peak shows that $[\text{Fe}/\text{H}]$ of this stream is about -2.05 . The distance to this piece of the stream is $8.0 \pm 0.53 \text{ kpc}$.

Region 6, Plates 2390 and 2410: A strong and narrow peak is detected in Figure 9, at $v_{gsr} = -87 \pm 2 \text{ km s}^{-1}$, $\sigma = 9 \text{ km s}^{-1}$ and $g_0 = 18.82$. $[\text{Fe}/\text{H}]$ distributions show the metallicity peaks at about -2.05 , which is consistent with the $[\text{Fe}/\text{H}]$ peak found in plate 2567 and slightly higher than plate 2914, this indicates that they are from the same stream. A distance estimate puts stars in this region of the stream at $8.8 \pm 0.75 \text{ kpc}$ from the sun.

Region 1, Plate 1154: This is a special SDSS legacy plate, rather than a SEGUE plate, but since it is at low Galactic latitude it does have a large number of stellar candidates. Its important GD-1 stream candidate stars cluster at velocity $v_{gsr} = 108 \pm 5 \text{ km s}^{-1}$, with $\sigma_v = 11 \text{ km s}^{-1}$, and (lower S/N) metallicity $[\text{Fe}/\text{H}] = -2 \pm 0.3$, which anchors the stream orbit away from regions 4,5 and 6. With larger errors, the distance to this stream here is $10.4 \pm 1.2 \text{ kpc}$. There is a second peak (3 stars) at $v_{gsr} = -40 \text{ km s}^{-1}$. We discount this second peak as being associated with GD-1, since two of its three members have $[\text{Fe}/\text{H}] =$

-1.8, significantly higher than the average for other stream peak members. This secondary peak could be related to the Anti-Center stream noted by Grillmair, Carlin and Majewski (2008), as the radial velocity of these stars is $RV \sim +112 \text{ km s}^{-1}$, is close to their value for ACS-C (see lower panel of Figure 1 and Figure 2 of that work).

4.2. Other Regions

The following 3 regions were not involved in the model fit (see below), but as there are SEGUE spectra available here along the orbit defined by the imaging arc defined in Equation 1, we examine these SEGUE plates for possible stream members.

Region 2, Plates 1760, 2433, 2667 and 2671: This plate pair was targeted by SEGUE as it contains the open solar-metallicity cluster M67. The Sagittarius stream also passes near by, along with the Anti-center stream. By chance, the GD-1 stream arc appears to pass within 1.3° of the plate center, and several very low metallicity turnoff stars are detected with average $v_{gsr} = 69 \text{ km s}^{-1}$. The distance to the stream is $6.5 \pm 0.64 \text{ kpc}$.

Region 3, Plates 2304 and 2319: Several stars with metallicity have velocities in a broad excess near $v_{gsr} = 42 \text{ km s}^{-1}$, however there is not a significant candidate peak here. A peak at $v_{gsr} \sim -105 \text{ km s}^{-1}$ has stars with $< [\text{Fe}/\text{H}] > \sim -1.8$, and is not a viable stream maximum. The distance from section 3 is estimated at $7.0 \pm 0.36 \text{ kpc}$.

Region 7, Plate 2539 and 2547: This plate pair is on the fitted arc of Equation 1, but the stream becomes too tenuous to be defined. We do not see a velocity peak here, but following the trend in the peaks of points 1-6 there may be two or three stars (above background) at $v_{gsr} = -156 \pm 10 \text{ km s}^{-1}$, with the correct metallicity and proper motion to be associated with GD-1. We do not place as strong a confidence in the GD-1 membership of stars in this peak as the other 6 regions. A very uncertain distance estimate to the stream here, is about $d = 9.9 \pm 1.2 \text{ kpc}$ from the Sun. Orbit fits, which were not fit to data in region 7, confirm that this is the correct velocity to be looking for stream stars, but that the distance is somewhat underestimated.

We note that the estimated distances to individual regions are in very good agreement with those quoted by Grillmair and Dionatos (2006), indicating that the results are somewhat robust to details of the method and potential parameters.

5. The Observed Stream Properties

The observed properties of the stars in the seven GD-1 stream candidate regions are summarized in Table 1, where we list region number (N); Equatorial coordinates, (α, δ) ; the corresponding Galactic coordinates (l, b) with errors (we use δ to denote a measured error, to distinguish it from the intrinsic dispersion, which we denote with the symbol σ); the average Galactocentric standard of rest velocity and heliocentric radial velocity with an error, and the velocity dispersion. The velocity mean and dispersion were calculated as described in §3. The tabulated intrinsic dispersions are upper limits to the actual velocity dispersion of the stream; since they are similar in size to the velocity errors for each individual spectrum, the measurement is consistent with an intrinsic velocity distribution of zero. The error in the mean is the velocity dispersion divided by the square root of the number of stars used to compute it. Regions 2, 3, and 7 do not have clear, narrow peaks in the velocity distributions and therefore were not used to fit the orbit, though Figure 6 shows there are excess stars at about the right velocities.

Table 1 lists the computed Galactic X, Y, Z positions (with respect to a right handed coordinate system with the Sun at $(-8, 0, 0)$ kpc) for each stream region and a distance to the stream at that region, again with errors. For the four regions numbered 1, 4, 5 and 6, the velocity and position accuracies are highly significant, and there is high confidence of the GD-1 stream membership of stars highlighted in the corresponding boxes of Figure 6.

Figure 10 highlights this confidence by showing a color-magnitude diagram of all high-confidence spectroscopic GD-1 stream candidates in regions 1-7, shifted to a standard distance of 9 kpc based on the photometric Hess diagram fitting. These objects are also proper motion selected, in that only objects within $\pm 2\sigma$ of the proper motion of the best fit model are kept. Superimposed over the spectral candidates is the M92 fiducial sequence of An et al. (2008) shifted to a distance modulus of $m - M = 14.76$, identical to that used in Figure 1. Distances to the other regions were estimated as described in section 3.

We now calculate our best metallicity estimate for GD-1 by selecting only the 48 stars with spectra in Figure 10. We note that these stars were pre-cut on metallicity at an earlier stage (Figure 6) to have $-2.3 < [\text{Fe}/\text{H}] < -1.65$. A histogram with bins similar to the measurement error yields a GD-1 stream metallicity of $[\text{Fe}/\text{H}] = -2.1 \pm 0.1$ dex with a dispersion of $\sigma = 0.3$ dex (essentially the measurement error). In addition to these statistical errors, there may be systematic errors in the metallicity determinations from SDSS DR7 of ~ 0.2 dex (Allende Prieto et al. 2008).

6. Orbit Fitting

We now use the data listed in Table 1 to fit an orbit for the stream, assuming a fixed Galactic potential. Grillmair and Dionatos (2006) postulated the progenitor of this stream is a globular cluster because it has a narrow width in the sky. As a cluster orbits the Galaxy, stars farther from the progenitor will depart from the orbit due to dynamical friction and scattering of the stream stars. Because the progenitor is presumed to be a compact object with a few km s^{-1} velocity dispersion, it is reasonable to assume that the stars in the tidal stream lie approximately on the orbit of the globular cluster (Odenkirchen et al. 2003). Dwarf galaxies, on the other hand, will experience larger spatial dispersions because they have larger dispersions in their energies. Therefore, in this paper, we fit the orbit to the positions and velocities of the stars in the tidal stream.

6.1. Galactic Model

The Galactic potential model used in this work follows directly from Law et. al. (2005). We use a 3 component potential - disk, bulge, and halo, of the form given in Equations (7), (8), and (9).

$$\Phi_{disk} = -\alpha \frac{GM_{disk}}{\sqrt{R_c^2 + (a + \sqrt{Z^2 + b^2})^2}} \quad (7)$$

$$\Phi_{bulge} = -\frac{GM_{bulge}}{r + c} \quad (8)$$

$$\Phi_{halo} = v_{halo}^2 \ln \left(R_c^2 + \frac{Z^2}{q^2} + d^2 \right) \quad (9)$$

In these potentials, $R_c^2 = X^2 + Y^2$ and $r^2 = X^2 + Y^2 + Z^2$, where (X, Y, Z) are Galactocentric Cartesian coordinates. We adopt the Sun - Galactic center distance so that $X_{Sun} = -8.0$ kpc. The symbol R_c is the cylindrical radius from the center of the Galaxy, whereas R refers to the Sun-centered distance to an arbitrary point along the stream. In these potentials, M_{disk} and M_{bulge} are the masses of the disk and bulge, respectively. The spatial extent of the potentials are determined by a , the disk scale length, b the disk scale height, c the bulge scale radius, and d the dark matter halo scale length. Additionally, v_{halo} describes the dark matter halo dispersion speed (which is related to the total dark matter halo mass), and q represents the dark matter halo flattening in the Z direction. We found that the parameters

of the Galactic potential were not well constrained by the path of the tidal stream, so these parameters (Table 3) were held constant, with the same values used by Law et. al. (2005).

In this work, we will fit four orbital parameters, given in Table 4. $(R_5, v_{x,5}, v_{y,5}, v_{z,5})$ are the distance (from the Sun) to, and velocities of, region 5. Given a Galactic potential, these parameters fully specify the GC orbit. We then evolve the test particle forward and backward from the starting location, using the *mkorbit* and *orbint* tools in the NEMO Stellar Dynamics Toolbox (Teuben 1995). We convert the resulting orbit into (l, b) and perform the goodness of fit calculation.

To find reasonable initial values for these parameters, we imagine placing a test particle in region 5 at $(l, b, R_5) = (172.3^\circ, 57.43^\circ, 8.0 \text{ kpc})$. We then construct a vector between the $(l, b, R_5) = (172.3^\circ, 57.43^\circ, 8.0 \text{ kpc})$ and $(l, b, R_6) = (161.95^\circ, 59.12^\circ, 8.8 \text{ kpc})$ points. This gives us the direction of the total velocity, because we are assuming the orbit passes through both of these points. The principle initial values for the parameters in region 5 are $(R_5, v_{x,5}, v_{y,5}, v_{z,5}) = (8.0 \text{ kpc}, -94 \text{ km/s}, -285 \text{ km/s}, -104 \text{ km/s})$. In practice we start searching for the best parameters in a range of values near these approximate values for the orbital parameters. The parameter selection ranges are given in Table 4.

6.2. Goodness-of-Fit

In order to find the best-fit orbit to the data given in Table 1, it is necessary to define a goodness-of-fit metric, and search the relevant parameters for the minimum value of this metric. The metric for an orbit of this type involves three important factors: the orbit passing through the plate locations in the sky, having the proper velocities at these locations, and having the correct distances. In order to consider all of these factors, we define three chi-squared values, one for each of the relevant variables, and simply sum them to create the total goodness of fit metric. Specifically,

$$\chi_b^2 = \sum_i \left(\frac{b_{model,i} - b_{data,i}}{\sigma_b} \right)^2, \quad (10)$$

$$\chi_{rv}^2 = \sum_i \left(\frac{rv_{model,i} - rv_{data,i}}{\sigma_{rv,i}} \right)^2, \quad (11)$$

$$\chi_R^2 = \sum_i \left(\frac{R_{model,i} - R_{data,i}}{\sigma_{R,i}} \right)^2, \text{ and} \quad (12)$$

$$\chi^2 = \frac{1}{\eta} (\chi_b^2 + \chi_v^2 + \chi_R^2), \quad (13)$$

where $\eta = N - n - 1$, N being the number of data points, and n being the number of parameters.

To calculate these χ^2 values, we calculate a model orbit using the selected parameters. We search the orbit for the l values from the plates, and use the associated values of b , v_{gsr} , and R to compute χ^2 .

6.3. Gradient Descent

We now optimize the orbital parameters so that χ^2 is minimized. To do this, we choose an initial set of parameters, calculate an orbit using the NEMO Stellar Dynamics Toolbox (Teuben 1995), and calculate χ^2 . We then use a gradient descent method to adjust the parameters to new values, generate a new orbit, and recalculate χ^2 . This process is continued until the true minimum value of χ^2 is found, and the associated parameters describe the best fit orbit.

Let the vector $\vec{Q} = (R_5, v_{x,5}, v_{y,5}, v_{z,5})$ describe the parameters. For each \vec{Q} there is an associated $\chi^2(\vec{Q})$. We choose an initial set of parameters \vec{Q}_0 , and find $\chi^2(\vec{Q}_0)$. We then iterate the parameters by Equation (14).

$$Q_{i,new} = Q_{i,old} - h_i \Lambda \vec{\nabla}_i \chi^2(\vec{Q}_{old}) \quad (14)$$

We calculate the gradient using a finite difference method, shown in Equation (15).

$$\nabla_i \chi^2(\vec{Q}) \approx \frac{\chi^2(Q_i + h_i) - \chi^2(Q_i - h_i)}{2h_i} \Big|_{\text{all other } Q_k \text{ fixed}} \quad (15)$$

Different values of h_i are used because the parameters are on different scales, it would not be appropriate to use the same step size for them all. The step sizes for the parameters are given in Table 4.

Λ is a variable-learning parameter. It initially begins at $\Lambda = 1$, and if the new value of $\chi^2(\vec{Q})$ is smaller than the old, then Λ is multiplied by 1.03, if not, it is multiplied by 0.80. The purpose of this is to ensure if a minimum is being found, then it is found faster than with a constant-learning parameter. We also multiply it by the associated h_i value to make the step size appropriate for the parameter being considered.

6.4. Error Estimation

The uncertainties of the best-fit parameters can be estimated from the shape of the χ^2 surface at its minimum. To do this, we follow the method outlined by Cole et al. (2008). We construct a matrix \mathbf{V} of second partial derivatives of the χ^2 surface, evaluated at the minimum found by the gradient descent. The error estimate for the i^{th} parameter is $\sigma_i = \sqrt{2V_{ii}}$. The \mathbf{V} matrix is defined as

$$\mathbf{V} \equiv \mathbf{H}^{-1}. \quad (16)$$

The matrix \mathbf{H} is the Hessian Matrix, whose elements are given by

$$\begin{aligned} H_{ij} &= \frac{H_{ij}^1 - H_{ij}^2 - H_{ij}^3 + H_{ij}^4}{4h_i h_j}, \text{ where,} \\ H_{ij}^1 &= \chi^2(Q_j + h_j, Q_i + h_i) \Big|_{\text{all other } Q_k \text{ fixed}} \\ H_{ij}^2 &= \chi^2(Q_j - h_j, Q_i + h_i) \Big|_{\text{all other } Q_k \text{ fixed}} \\ H_{ij}^3 &= \chi^2(Q_j + h_j, Q_i - h_i) \Big|_{\text{all other } Q_k \text{ fixed}} \\ H_{ij}^4 &= \chi^2(Q_j - h_j, Q_i - h_i) \Big|_{\text{all other } Q_k \text{ fixed}} \end{aligned} \quad (17)$$

(18)

7. Results and Discussion

We select five initial sets of parameters by randomly choosing values within the ranges given in Table 4. We perform the gradient descent to reach the best fit parameters. We then estimate the parameter errors using the Hessian method outlined above. The best-fit parameters and their errors are $(R_5, v_{x,5}, v_{y,5}, v_{z,5}) = (8.4 \pm 0.8 \text{ kpc}, -89 \pm 2 \text{ km/s}, -236 \pm 6 \text{ km/s}, -115 \pm 3 \text{ km/s})$. The chi-squared of this fit is 2.07. The negative velocities indicate a retrograde orbit. The perigalacticon for this orbit is located $r = 14.43 \pm 0.5 \text{ kpc}$ from the Galactic center at $(l, b) = (158^\circ, 60^\circ)$, near region 6. The space velocity of stars in the model at this position is 276 km s^{-1} . The apogalacticon is at $r = 28.7 \pm 2 \text{ kpc}$ from the Galactic center, toward $(l, b) = (306^\circ, -35^\circ)$, though we do not observe this direction on the sky. All errors are 1σ .

These orbital parameters are fairly insensitive to the choices of parameters in the Galactic potential. In particular, they are good estimates of the orbital parameters for a wide range

of q and d . To investigate whether we could determine anything about the shape of the dark matter halo from this tidal tail, we performed parameter sweeps on q and d while keeping the kinematic parameters constant (Figure 11). We see that very low flattenings are inconsistent with the data, but a wide range of q and d are allowed.

The potential assumed in fitting the orbit is a standard logarithmic flat-rotation curve dark matter halo plus a stellar disk. Since the GD-1 stream approaches within 15 kpc of the Galactic center, the effects of the massive disk are felt by the orbit, and increasing the relative mass of the disk vs. the halo can mimic the effects of a flattened halo. At perigalacticon, the disk exerts twice as much gravitational force as the halo. Given this, it is not surprising that the stream orbit depends minimally on the halo parameters. More models and constraints, from this and other streams, are clearly needed to constrain the shape of the dark matter halo.

The upper panel of Figure 12 shows the orbit in (l, b) with the stream locations shown. The model prediction is in very good agreement with the experimental observations. The middle and lower panels of Figure 11 show the orbit in l versus v_{gsr} and l versus distance from the Sun. We also see good agreement with the experimental observation. Figure 13 shows the orbit projected into the three planes of Galactic coordinates (X, Y, Z) . We deduce an orbital eccentricity $e = 0.33 \pm 0.02$ (one sigma error) and an inclination to the Galactic plane of $i \sim 35 \pm 5^\circ$. Arrows show the relative direction of the stream’s retrograde motion compared to the Milky Way.

The final columns of Table 1 show the predicted proper motions (μ_l, μ_b) for stars in the stream at each region 1-7 based on the distances in Table 1. These predictions may be compared with actual observed proper motions for stream star candidates in Table 2 at each region. In general the agreement is quite good for regions 2-6, given proper motion errors of $1\sigma = 3 \text{ mas yr}^{-1}$ in each coordinate. Spectral candidates more than 2σ away were excluded from Figure 10, dropping about 20% of the candidates, leaving a generally good fit to a shifted M92 fiducial sequence for these regions. Region 7 had fewer good proper motion matches, and it is possible that we are not seeing GD-1 stream candidates here.

Figure 14 shows the photometrically chosen stars with proper motions available near regions 1,4,5 and 6, along with an equivalent set of field stars (chosen 5 degrees away) for comparison. There’s a clear excess of ‘on-stream’ stars in the lower right quadrant of each region on-stream – these are likely stream members. The estimated tangential velocities (relative to the Sun) are given.

To search for a possible progenitor, we selected all Milky Way globular clusters from Harris (1996) that had metallicities in the range $-2.5 < [\text{Fe}/\text{H}] < -1.5$. Only seven of these

globular clusters (Terzan 8, Arp2, NGC 6809, NGC 6749, NGC 6341, NGC 6681, and NGC 6752) are within 5° of the GD-1 orbit. Additionally, we considered NGC 2298, which is 5.5° from the orbit, and has a metallicity of $[\text{Fe}/\text{H}] = -1.85$. We compared the positions and velocities of these globular clusters with an orbital path that extends all the way around the Milky Way. To create a stream of this length would require a globular cluster to orbit the Milky Way for on the order of gigayears, with the length depending on the concentration of the progenitor, as well as the shape and location of the progenitor’s orbit. Of the eight globular clusters, NGC 6809, NGC 6749, and NGC 6752 are ruled out because their distances are more than a factor of two different from the distance to the orbit. The remaining five clusters had radial velocities that are inconsistent with the predicted orbit by more than 50 km/s. We therefore conclude that the Milky Way globular cluster catalog published by Harris (1996) does not contain the progenitor of this stream.

8. Conclusions

We use spectroscopic kinematic and abundance information to isolate stars in the GD-1 stream, and use the positions and velocities of those stars to derive orbital parameters for its orbit. The GD-1 stream is moving very rapidly on a retrograde orbit around the Milky Way. In the region of the orbit which is detected, it has a distance of about 7-11 kpc from the Sun. The stream’s orbit takes it to apogalactic distances of 28.75 ± 2 kpc, and it has a perigalacticon of 14.43 ± 0.5 kpc, implying an eccentricity of 0.33 ± 0.02 . The inclination to the Galactic plane is about $i \sim 35^\circ \pm 5$. The metallicity of the stream is $[\text{Fe}/\text{H}] \sim -2.1 \pm 0.1$ plus systematic errors of a few tenths dex. None of the known globular clusters in the Milky Way have positions, radial velocities, and metallicities that are consistent with being the progenitor of the GD-1 stream.

The consistency between the proper motions of these stream candidates and our best fit model gives us further confidence that we have identified stream members and that our model accurately represents the path on the sky of the stream stars. While we claim only consistency here between the proper motion data and our model, we note that more detailed fits to the proper motion (in addition to the radial velocities) for such nearby streams can be a crucial tool in constraining the halo potential shape and other parameters.

We acknowledge a careful reading and several important suggestions from the anonymous referee which significantly improved the observational analysis section of this paper. B.A.W and H.J.N. acknowledge support from the National Science Foundation, grant AST 06-06618. We gratefully acknowledge Peter Teuben for many useful NEMO discussions and Lee Newberg for assisting us with calculating the measurement errors. We also acknowledge

useful discussion with Linda Sparke regarding streams in potentials. Z.H.T. acknowledges support from the National Natural Science Foundation of China under Grant No. 10778711. T.C.B. has received partial support for this work from grants PHY 02-16783 and PHY 08-22648: Physics Frontiers Center / Joint Institute for Nuclear Astrophysics (JINA), awarded by the U.S. National Science Foundation.

Funding for the SDSS and SDSS-II has been provided by the Alfred P. Sloan Foundation, the Participating Institutions, the National Science Foundation, the U.S. Department of Energy, the National Aeronautics and Space Administration, the Japanese Monbukagakusho, the Max Planck Society, and the Higher Education Funding Council for England. The SDSS Web Site is <http://www.sdss.org/>.

The SDSS is managed by the Astrophysical Research Consortium for the Participating Institutions. The Participating Institutions are the American Museum of Natural History, Astrophysical Institute Potsdam, University of Basel, Cambridge University, Case Western Reserve University, University of Chicago, Drexel University, Fermilab, the Institute for Advanced Study, the Japan Participation Group, Johns Hopkins University, the Joint Institute for Nuclear Astrophysics, the Kavli Institute for Particle Astrophysics and Cosmology, the Korean Scientist Group, the Chinese Academy of Sciences (LAMOST), Los Alamos National Laboratory, the Max-Planck-Institute for Astronomy (MPIA), the Max-Planck-Institute for Astrophysics (MPA), New Mexico State University, Ohio State University, University of Pittsburgh, University of Portsmouth, Princeton University, the United States Naval Observatory, and the University of Washington.

REFERENCES

- Abazajian, K. et al., 2009, ApJS, submitted, arXiv:0812.0649
- Adelman-McCarthy, J.K., Agüeros, M.A., Allam, S.S. et al., 2008, ApJS, 175, 297
- Allende Prieto, C. et al. 2008 AJ, 136, 2070.
- An, D., Johnson, J.A., Clem, J. L., et al., 2008, ApJS, in press, arXiv:0808.0001
- Bellazzini, M., Ferraro, F., and Ibata, R. 2002, AJ, 125, 188B
- Belokurov, V., et al. 2007, ApJ, 658, 337
- Bullock, J. S., & Johnston, K. V. 2005 ApJ 635, 931
- Chapman, S. C. et al. 2008, MNRAS, submitted, arXiv:0808.0755
- Clem, J. L., Vanden Berg, D. A., & Stetson, P. B. 2008 AJ 135, 682
- Cole, Nathan, et al. 2008, ApJ, 683, 750
- Duffau, S., Zinn, R., Vivas, A. K., Carraro, G., Mendez, R. A., Winnick, R., & Gallart, C. 2006, ApJ, 636, L97
- Fellhauer, M., Belokurov, V., Evans, W. et al. 2006, ApJ, 651, 167
- Ferguson, A. M. N., Johnson, R. A., Faria, D. C., Irwin, M. J., Ibata, R. A., Johnston, K. V., Lewis, G. F., & Tanvir, N. R. 2005, ApJ, 622, L109
- Fukugita, M., Ichikawa, T., Gunn, J.E., Doi, M., Shimasaku, K., and Schneider, D.P. 1996, AJ, 111, 1748
- Grillmair, C. J. & Dionatos, O. 2006, ApJ, 643, L17 (GD)
- Grillmair, C. J. 2006, ApJ, 645, L37
- Grillmair, C. J., & Johnson, R. 2006, ApJ, 639, L17
- Grillmair, C. J. 2006, ApJ, 651, L29
- Grillmair, C. J., Carlin, J. L. & Majewski, S. R. 2008, ApJ, 689, L117
- Grillmair, C. J. arXiv:0811.3965, ApJ, in press.
- Gunn, J.E., et al. 1998, AJ, 116, 3040

Gunn, J.E., et al. 2006, AJ, 131, 2332

Harris, W. E. 1996, AJ, 112, 1487

Helmi, A., 2004, ApJ, 610, L97

Hogg, D. W., Finkbeiner, D.P., Schlegel, D.J., and Gunn, J.E. 2001, AJ, 122, 2129

Ibata, R. A., Gilmore, G., and Irwin, M.J. 1995, MNRAS, 277, 781

Ibata, R. , Irwin, M., Ferguson, A. M. N., Lewis, G. F., Tanvir, N. 2001 Nature 412, 49

Ibata, R., Lewis, G. F., Irwin, M., Totten, E., and Quinn, T. 2001, ApJ, 551, 294

Ivezic, Z., et al. 2004, AN, 325, 583

Law, David R., Johnston, Kathryn V., and Majewski, Steven R. 2005, ApJ, 619, 807

Lee, Y. S., et al. 2008a, AJ, 136, 2022

Lee, Y. S., et al. 2008b, AJ, 136, 2050

Leon, S., Meylan, G., and Combes, F. 2000, AAP, 359, 907

Majewski, Steven R., Skrutskie, M. F., Weinberg, Martin D., Ostheimer, James C. 2003, ApJ, 549, L199

Martinez-Delgado et al. 2001, ApJ, 549, L199

Martinez-Delgado et al. 2008, ApJ, submitted, arXiv:0801.4657

Martinez-Delgado, D., Gabany, R. J., Pennarrubia, J., Rix, H.-W., Majewski, S. R., Trujillo, I., & Pohlen, M. , in "Highlights of Spanish Astrophysics V", Proceedings of the VIII Scientific Meeting of the Spanish Astronomical Society (SEA), Springer, arXiv:0812.3219

Munn, J. A. et al. 2004 AJ 127, 3034

Newberg, H.J., Yanny, B., et al. 2002, ApJ, 569, 245

Newberg, H.J., Yanny, B., Cole, N., et al., 2007, APJ, 668, 221

Odenkirchen, M., et al. 2001, ApJ, 548, L165

Odenkirchen, M., et al. 2003, AJ, 126, 2385

Pier, J.R., Munn, J.A., Hindsley, R.B., Hennessy, G.S., Kent, S.M., Lupton, R.H., and Ivezić, Z. 2003, AJ, 125, 1559

Rockosi, C.M., Odenkirchen, M., Grebel, E.K. et al., 2002, AJ 124, 349

Schlegel, D.J., Finkbeiner, D.P., & Davis, M. 1998, ApJ, 500, 525

Sirko, E. et al. 2004 AJ 127, 899

Smith, J.A., et al. 2002, AJ, 123, 2121

Stoughton, C., et al. 2002, AJ, 123, 485

Teuben, P.J. The Stellar Dynamics Toolbox NEMO, in: Astronomical Data Analysis Software and Systems IV, ed. R. Shaw, H.E. Payne and J.J.E. Hayes. (1995), PASP Conf Series 77, p398.

Tucker, D., et al. 2006, AN, 327, 821

Vivas, A. K. et al. 2001, ApJ, 554, L33

Yanny, B., Newberg, H. J., et al. 2000, ApJ, 540, 825

Yanny, B., Rockosi, C., Newberg, H., Knapp, G. et al. 2009 AJ, submitted.

York, D.G. et al. 2000, AJ, 120, 1579

Fig. 1.— The GD-1 stream Hess diagram

Hess diagram of on-stream minus off-stream (taken from 5 degrees lower δ than the on-stream stars) star counts. Darker areas of the figure have higher stellar density. Thick disk stars and M dwarfs did not subtract perfectly between on and off regions. The blue turnoff at $((g - r)_0, g_0) = (0.25, 19)$ indicates that the GD-1 stream is relatively metal poor. A fiducial sequence for globular cluster M92 from Clem, Vanden Berg, & Stetson (2008), shifted to $m - M = 14.76$, is overlaid with black dots. The region of color-magnitude space used to select the photometry of stars in Figure 2 is outlined in heavy black lines. The region of color-magnitude space that is used to select the stars plotted in Figure 3 is outlined in light black lines.

Fig. 2.— The GD-1 stream photometry

The upper panel shows a Hess diagram of stars in the SDSS footprint which are within the color and magnitude boxes thickly outlined in Figure 1. The GD-1 stream arcs faintly from $(\alpha, \delta) = (220^\circ, 58^\circ)$ to $(126^\circ, 0^\circ)$. Seven regions where spectroscopy of GD-1 stream star candidates have been obtained are numbered. Squares indicate regions where the stream was clearly found in velocity, and circles indicate additional plates that may contain stream stars. The lower panel shows the GD-1 stream in Galactic polar coordinates. The color-magnitude cuts are similar to the above, but plotted in Galactic polar coordinates as labeled. Note the stream's path on the sky.

Fig. 3.— Velocities of stars near the stream

We plot the line-of-sight, Galactocentric standard of rest velocity versus Galactic longitude for SEGUE and SDSS stars for which we have spectra, and which are close in color-magnitude space to the fiducial sequence of M92 (as indicated by the narrow dark outlines in Figure 1), which are close (within 1.3°) in projected distance to the GD-1 stream shown in Figure 2. A sine curve with amplitude 110 km s^{-1} is shown to indicate the locus of stars rotating with the Sun about the Galactic center. Stars in the halo will have velocities centered on $v_{gsr} = 0$ and a large $\sigma \sim 100 \text{ km s}^{-1}$ dispersion. Regions where GD-1 stream candidates are followed up on are numbered 1-7. Note in particular the groups of stars at $v_{gsr} \sim -90 \text{ km s}^{-1}$ in regions 5 and 6.

Fig. 4.— Histogram of v_{gsr} towards regions 5, 6

All stars with spectra from Figure 3 towards regions 5, 6 of Figure 2 are histogrammed in Galactocentric velocity. Gaussians are overlaid representing a thick disk and halo distribution toward this direction. The candidate GD-1 stream stars at about $v_{gsr} \sim -82 \text{ km s}^{-1}$ cannot be explained by either a halo or thick disk distribution.

Fig. 5.— Metallicity distribution of region 5,6 stars

Histogram of SSPP metallicities for all stars (light line) and for stars with $-97 < v_{gsr} < -61$ km s⁻¹ (heavy line). The velocity-selected peak has an excess of stars with metallicity lower than that of the halo. The hashed line indicates a correction to the heavy line for interlopers at other velocities which have the same metallicities as candidate stream stars. This figure suggests that the peak metallicity of the GD-1 stars is lower than $[Fe/H]=-1.9$.

Fig. 6.— Velocity distribution of low metallicity stars near the stream

The subset of stars from Figure 3 with SSPP metallicities $-2.3 < [Fe/H] < -1.65$ are presented. Now the counter-rotating GD-1 stream stars stand out more clearly against their field contaminants compared with Figure 3. Regions 1,4,5 and 6 have clear peaks; the mean and the error on the mean for these peaks are indicated by the position and height of the rectangles at these four longitude locations. The circles in regions 2, 3, and 7 indicate the area through which the stream should pass if our model is correct. All areas except region 7 seem to have an excess of stars with the expected stream velocities.

Fig. 7.— Background Subtracted Hess diagrams along the stream

At each region 1-7, stars with $(u - g)_0 > 0.4$ within 0.5° of the cubic described by equation 1 are selected. A similar background set of stars, obtained from a region 1.5° away from the cubic, was selected for each of the seven regions. The Hess diagrams show the stream star counts minus the background star counts, as a function of g_0 and $(g - r)_0$. Light (white) regions indicate an excess of stars along the stream.

Fig. 8.— Hess diagrams with fits

The diagrams from the previous figure are fitted with M92 fiducial loci, shown as (green) crosses, shifted up and down in magnitude until a maximum correlation is obtained (see text). Candidate stream stars with spectra are indicated as (red) diamonds. The distance to each region along the stream is then derived from the best fitting shifted M92 fiducial.

Fig. 9.— Velocity selection of stream candidates

Velocity histograms in each GD-1 stream candidate regions 1-7, with SSPP metallicities $-2.3 < [Fe/H] < -1.65$. A Gaussian with $\sigma = 100$ km s⁻¹ is overlaid. The v_{gsr} of the expected GD-1 peak is noted in each panel.

Fig. 10.— Stars with spectra in the stream

All stars in regions 1-7 with SEGUE spectra which meet the metallicity, color, magnitude, velocity and proper motion cuts as described in the text are plotted with colored

points as indicated in the legend, along with estimated distance to each set of points. Each set of points was shifted to the reference distance of 9 kpc (of Figure 1), and overlaid with a M92 fiducial locus, shifted to the same distance moduli. Note the two (blue) points at $g_0 \sim 15.3$, which are actually at $g_0 \sim 14.9$ before shifting. These are candidate BHB stars in the GD-1 stream, at a distance of 7.5 kpc from the Sun in region 4.

Fig. 11.— Parameter Sweep of q and d

Fixing the orbital parameters at their best fit values, derived assuming that $q = 1$ and $d = 12$, we varied d and q and measured χ^2 . This is justified by our observation that the best fit GD-1 orbital parameters are fairly similar for a large range of assumed q values. The normalization of this χ^2 surface in d, q was chosen so that the χ^2 at $(d, q) = (12, 1)$ is 2, to match the optimization presented in this paper. The dark squares in the figure show the locus of lowest χ^2 in this two dimensional surface. We see that very low values of q are not favored, while there is almost no constraint on how prolate the dark matter distribution can be. The values of q and d are coupled. The best fit d for a given q shifts somewhat with small changes to the orbital parameters, so this plot cannot be used to definitively pin down the d value, even though the χ^2 surface seems narrow in that dimension.

Fig. 12.— Best Fit Orbit

Upper panel: Galactic coordinates. The best fit orbit (with fixed q, d) to the data in the four regions 1,4,5 and 6. Region 1 is leftmost, with $l = 224.47^\circ$. Galactic (l, b) for all seven regions described in the text are plotted as crosses. Middle panel, plotting Galactic longitude l vs. Galactocentric radial velocity v_{gsr} for the best fit model and data. Regions 1,4,5 and 6 (left-to-right) have the smallest error bars. Lower panel, plotting Galactic longitude l vs. Sun-centered distance to the stream. The errors on regions 4, 5 and 6 are small; the error bars on the other region data points are limited by how well the position of the stream turnoff (minus a background field) can be identified in a color-magnitude Hess density diagram of stream stars. The distance error bars are largest for region 7 (rightmost), where the stream is confusion limited.

Fig. 13.— Best Fit Orbit: X, Y, Z

Shown in heavy black line is the best fit orbit to the four regions 1,4,5 and 6 in Galactic rectangular coordinates (X, Y, Z) in each of the cardinal projections. The coordinate system is a right-handed system with the Sun at at $(-8,0,0)$ kpc and the Galactic center at the origin. The coordinate and turnoff magnitude data from the seven regions is converted to (X, Y, Z) assuming an absolute turnoff F star magnitude of $M_g = +4.2$. The seven points are indicated with error bars from distance error estimates. Regions 1 and 7 are indicated

in each panel, with the other regions falling in order at intermediate positions. The units of each axis is kpc. An arrow originating at the Sun indicates the direction of Galactic rotation. The arrows associated with the stream indicate the retrograde direction of motion of GD-1 stream stars. The space velocity of the stream at perigalacticon is approximately 276 km s^{-1} .

Fig. 14.— Proper Motion consistency

For the four regions $N=1,4,5,6$ where we have fitted the orbit, we select stars within 0.3° of a cubic similar to equation 1 which have measured USNO-B proper motions from the DR7 database. For reference, we select similar sets of field objects offset by 5 degrees in declination from the on-stream objects. We then sub-select stars with colors and magnitudes of stream turnoff candidates using the the heavily outlined box of Figure 1, and plot the μ_l vs μ_b of the on-stream (black dots) and off-stream (open circles) for each selected region. There is a clear excess of on-stream points extending to the lower right in each region. We superimpose crosses representing the point where the best fit model (Table 1) crosses the stream, and show the derived tangential velocity in the Figure. The cross always falls in the same quadrant with the excess of proper motion points. Typical errors on each point are 3 mas yr^{-1} in each direction. The upper and right axes in each figure convert the observed proper motions to tangential velocities, assuming the distance to the stars is the distance to the fitted orbit for that particular GD-1 stream region.

Table 1. GD-1 Stream Detections

N	α °	δ °	l °	δl °	b °	δb °	v_{gsr} km s ⁻¹	RV km s ⁻¹	δv km s ⁻¹	σ_v km s ⁻¹	X kpc	Y kpc	Z kpc	d kpc	δd kpc	μ_l mas/yr	μ_b mas/yr
1	126.58	-0.22	224.47	0.5	20.88	0.5	108	259	5	11	-14.86	-6.72	3.66	10.4	1.2	7.0	-6.4
2	131.92	11.17	215.93	0.2	30.83	0.2	69	188			-12.51	-3.27	3.32	6.5	0.6	8.6	-7.4
3	138.65	22.29	206.03	0.2	40.89	0.2					-12.75	-2.31	4.57	7.0	0.4	10.0	-7.3
4	144.25	30.09	197.00	0.2	47.54	0.2	-7	39	1	3.9	-12.83	-1.47	5.52	7.5	0.3	10.9	-6.5
5	157.92	44.19	172.30	0.2	57.24	0.2	-71	-88	2	5.3	-12.30	0.58	6.74	8.0	0.5	11.8	-2.4
6	163.69	48.32	161.95	0.2	59.02	0.2	-87	-124	2	9.2	-12.30	1.41	7.54	8.8	0.8	11.5	-0.6
7	217.50	57.51	99.95	1.0	55.00	1.0					-8.98	5.6	8.08	9.9	1.2	4.1	5.2

Table 2. Spectra of GD-1 Stream Candidates

SpecID	N	α °	δ °	v_{gsr} km s ⁻¹	$\sigma(v)$ km s ⁻¹	RV km s ⁻¹	g_0 mag	$(u - g)_0$ mag	$(g - r)_0$ mag	[Fe/H] dex	$\sigma([\text{Fe}/\text{H}])$ dex	log g dex	$\sigma(\text{logg})$ dex	μ_t mas/yr	μ_b mas/yr
1154-53083-266	1	125.683891	-0.439561	113.4	7.4	264.7	19.107	0.909	0.275	-1.89	0.08	3.46	0.25	3.5	-4.3
1154-53083-145	1	126.577150	-0.439386	97.8	7.8	249.4	19.102	0.904	0.180	-2.14	0.07	3.62	0.23	12.9	-10.5
1154-53083-155	1	126.645407	-0.340477	109.0	3.6	260.3	18.117	0.935	0.275	-2.06	0.04	3.30	0.22	11.6	-3.9
1760-53086-339	2	131.406984	9.770413	65.8	14.5	186.9	18.389	0.909	0.227	-2.18	0.11	4.05	0.29	9.4	-8.4
2671-54141-432	2	132.157853	11.135851	77.3	6.0	193.9	18.780	0.841	0.406	-2.24	0.04	3.54	0.22	10.0	-5.2
2667-54142-427	2	132.367656	11.325495	70.5	4.0	186.5	17.433	0.987	0.420	-2.17	0.02	2.77	0.24	6.7	-7.4
2667-54142-604	2	133.073392	12.266884	62.3	2.5	175.1	15.859	1.159	0.486	-2.08	0.03	2.22	0.15	8.4	-6.1
2319-53763-347	3	138.399875	22.413022	38.1	11.6	114.5	19.451	0.843	0.243	-2.24	0.22	3.80	0.09	13.2	-7.7
2319-53763-358	3	138.450751	22.434572	40.4	4.7	116.7	17.996	0.865	0.259	-1.93	0.02	3.90	0.10	12.5	-9.7
2319-53763-387	3	138.669378	22.559736	48.9	11.8	124.7	19.603	0.874	0.385	-2.07	0.07	3.68	0.30	12.1	-7.9
2889-54530-311	4	142.787815	29.461085	-0.9	4.2	47.8	17.454	0.972	0.417	-1.98	0.04	3.23	0.28	10.7	-9.4
2914-54533-297	4	142.978804	29.136307	-3.0	3.9	46.9	18.139	0.925	0.189	-2.09	0.04	3.94	0.16	8.8	-9.3
2889-54530-240	4	143.339524	29.620398	-6.2	4.7	41.7	17.933	0.883	0.256	-2.14	0.03	3.63	0.17	9.6	-6.7
2889-54530-204	4	143.424098	29.036453	-3.6	5.1	46.5	17.822	0.872	0.271	-2.21	0.05	3.28	0.20	6.7	-4.5
2889-54530-215	4	143.453188	29.120632	-3.4	1.7	46.4	14.981	1.194	-0.237	-2.09	0.11	3.20	0.17	9.5	-10.9
2889-54530-238	4	143.552948	29.477508	-4.3	4.6	44.1	17.843	0.888	0.293	-2.21	0.01	3.60	0.18	8.4	-9.1
2889-54530-225	4	143.597836	29.802697	-6.1	1.7	41.0	14.845	1.196	-0.102	-1.98	0.06	3.34	0.09	13.7	-11.1
2914-54533-171	4	143.718962	29.874100	-3.6	8.0	43.2	19.432	0.747	0.285	-2.26	0.08	3.33	0.56	15.4	-8.7
2914-54533-458	4	144.107345	30.737924	-9.8	4.8	33.6	18.716	0.779	0.216	-2.26	0.05	4.41	0.10	13.1	-6.5
2914-54533-453	4	144.120941	30.947724	-1.4	4.4	41.2	17.955	0.827	0.220	-2.10	0.02	3.79	0.28	14.3	-6.3
2914-54533-509	4	144.275720	30.280468	-4.4	3.9	40.6	18.292	0.909	0.187	-2.25	0.01	3.46	0.31	9.5	-12.2
2914-54533-515	4	144.487234	30.410401	-4.7	3.6	39.8	18.247	0.855	0.232	-1.82	0.04	3.72	0.15	10.5	-1.6
2914-54533-540	4	144.561728	30.968385	-1.9	11.0	40.4	20.190	0.854	0.344	-1.95	0.10	3.46	0.21	12.6	-3.8
2567-54179-396	5	157.181542	44.514349	-67.9	6.8	-85.0	18.745	0.841	0.254	-2.08	0.04	3.78	0.19	13.9	1.8
2567-54179-246	5	157.565788	43.643316	-73.0	6.0	-87.1	18.630	0.934	0.167	-2.23	0.01	3.71	0.18	12.9	-0.9
2567-54179-238	5	157.691771	43.797748	-71.9	12.7	-86.7	19.546	0.908	0.206	-2.21	0.02	3.27	0.16	10.1	-5.6
2567-54179-189	5	157.817344	43.923322	-70.1	11.9	-85.5	19.761	0.772	0.342	-1.88	0.07	4.23	0.36	9.0	3.5
2567-54179-211	5	157.889540	43.500286	-65.2	10.0	-79.0	19.309	0.901	0.205	-1.89	0.15	3.74	0.07	9.2	-0.3
2567-54179-212	5	158.051293	43.644022	-67.6	5.2	-82.1	18.349	0.839	0.208	-1.90	0.07	3.67	0.26	9.7	-0.2
2567-54179-170	5	158.137638	44.086320	-58.2	9.8	-74.4	19.112	0.863	0.201	-2.04	0.06	3.64	0.17	14.4	-1.7
2567-54179-491	5	158.437074	44.466389	-69.2	9.1	-87.1	18.242	0.880	0.209	-2.02	0.09	3.95	0.16	8.9	-1.9
2567-54179-511	5	158.700621	44.530392	-68.9	4.4	-87.2	18.083	0.954	0.237	-2.22	0.01	3.18	0.25	12.1	1.3
2557-54178-498	5	158.747249	44.686776	-74.2	3.9	-93.2	16.794	1.048	0.476	-2.12	0.02	2.60	0.27	13.5	2.7
2410-54087-297	6	162.371533	47.207633	-87.0	6.9	-118.3	18.893	0.885	0.255	-2.26	0.02	3.46	0.20	15.4	-1.3

Table 2—Continued

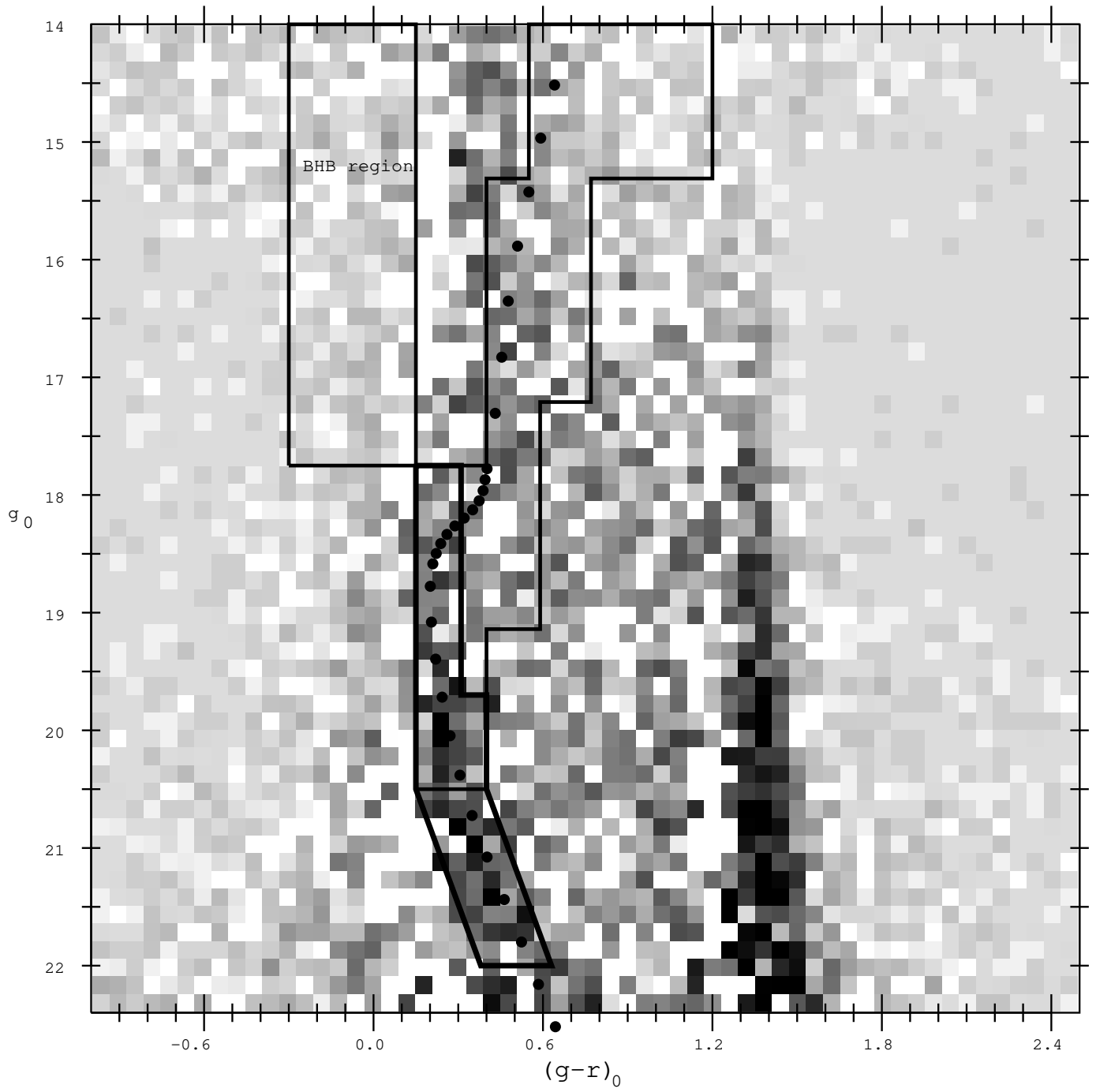
SpecID	N	α °	δ °	v_{gsr} km s ⁻¹	$\sigma(v)$ km s ⁻¹	RV km s ⁻¹	g_0 mag	$(u - g)_0$ mag	$(g - r)_0$ mag	[Fe/H] dex	$\sigma([\text{Fe}/\text{H}])$ dex	log g dex	$\sigma(\text{logg})$ dex	μ_l mas/yr	μ_b mas/yr
2410-54087-236	6	162.451620	48.002695	-85.2	4.2	-119.5	18.305	0.896	0.250	-1.71	0.04	3.51	0.21	8.6	4.8
2410-54087-288	6	162.547222	46.990942	-88.0	12.2	-118.7	19.344	0.893	0.164	-2.08	0.08	3.78	0.14	9.6	-3.8
2390-54094-256	6	162.557763	47.251097	-95.0	2.6	-126.6	16.945	1.048	0.036	-1.83	0.00	3.89	0.19	16.1	-1.5
2410-54087-380	6	162.743760	48.903984	-85.3	5.1	-123.1	18.632	0.840	0.269	-1.80	0.07	3.81	0.05	12.7	-1.6
2410-54087-173	6	163.799206	47.813588	-88.8	7.1	-123.6	18.828	0.845	0.200	-2.06	0.07	3.86	0.30	8.9	-1.8
2410-54087-539	6	164.064054	49.034036	-92.2	8.2	-131.6	19.293	0.925	0.169	-1.68	0.11	3.10	0.30	8.1	-1.7
2410-54087-501	6	164.334475	48.472850	-81.1	7.8	-118.8	19.401	0.925	0.202	-1.76	0.08	3.80	0.28	7.3	0.0
2410-54087-504	6	164.371325	48.224481	-90.6	8.8	-127.4	19.409	0.841	0.208	-1.75	0.07	4.30	0.14	11.3	-0.6
2390-54094-565	6	164.616981	49.202693	-81.1	2.0	-121.6	16.919	1.105	0.487	-1.86	0.01	2.93	0.19	6.9	3.7
2390-54094-615	6	165.199453	48.669262	-92.4	3.9	-131.5	17.895	0.896	0.385	-2.24	0.02	3.81	0.16	11.8	-1.7
2410-54087-637	6	165.381730	48.671045	-87.1	6.2	-126.4	18.928	0.887	0.206	-2.29	0.05	3.84	0.12	7.8	-0.2
2539-53918-406	7	217.430060	59.067783	-163.8	3.0	-297.5	15.805	1.226	-0.133	-2.11	0.03	3.29	0.12	5.9	3.7
2539-53918-070	7	219.681591	57.897316	-148.9	10.7	-283.7	17.970	0.862	0.199	-2.15	0.02	3.73	0.04	2.5	10.8
2539-53918-596	7	219.898491	58.258368	-157.6	5.5	-293.3	17.035	1.197	-0.167	-2.10	0.26	2.92	0.43	1.0	2.9

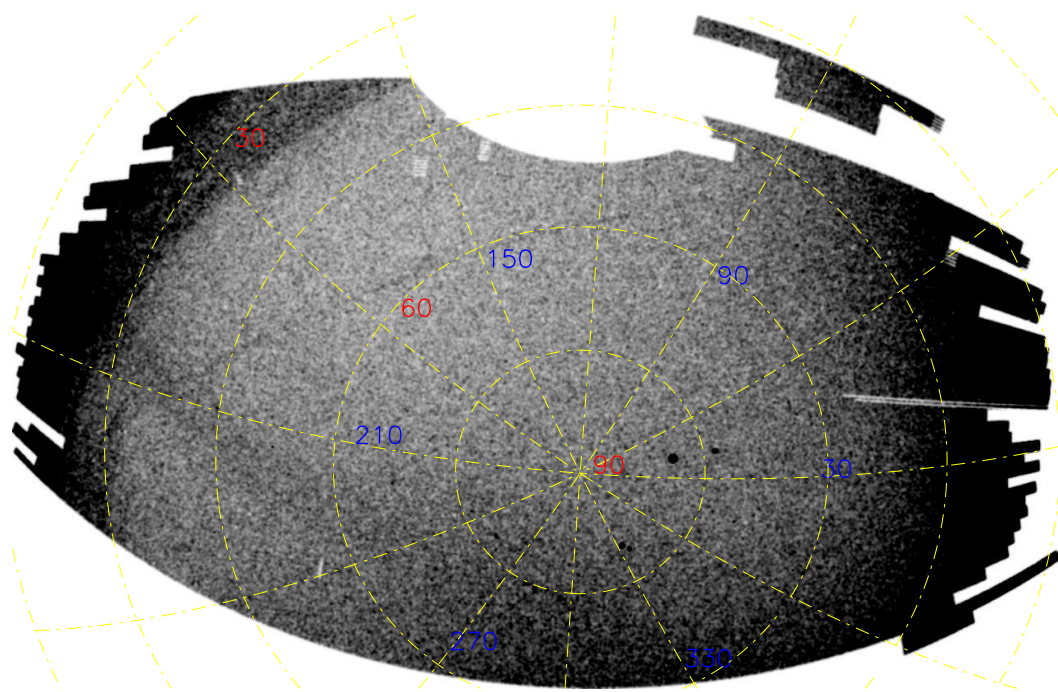
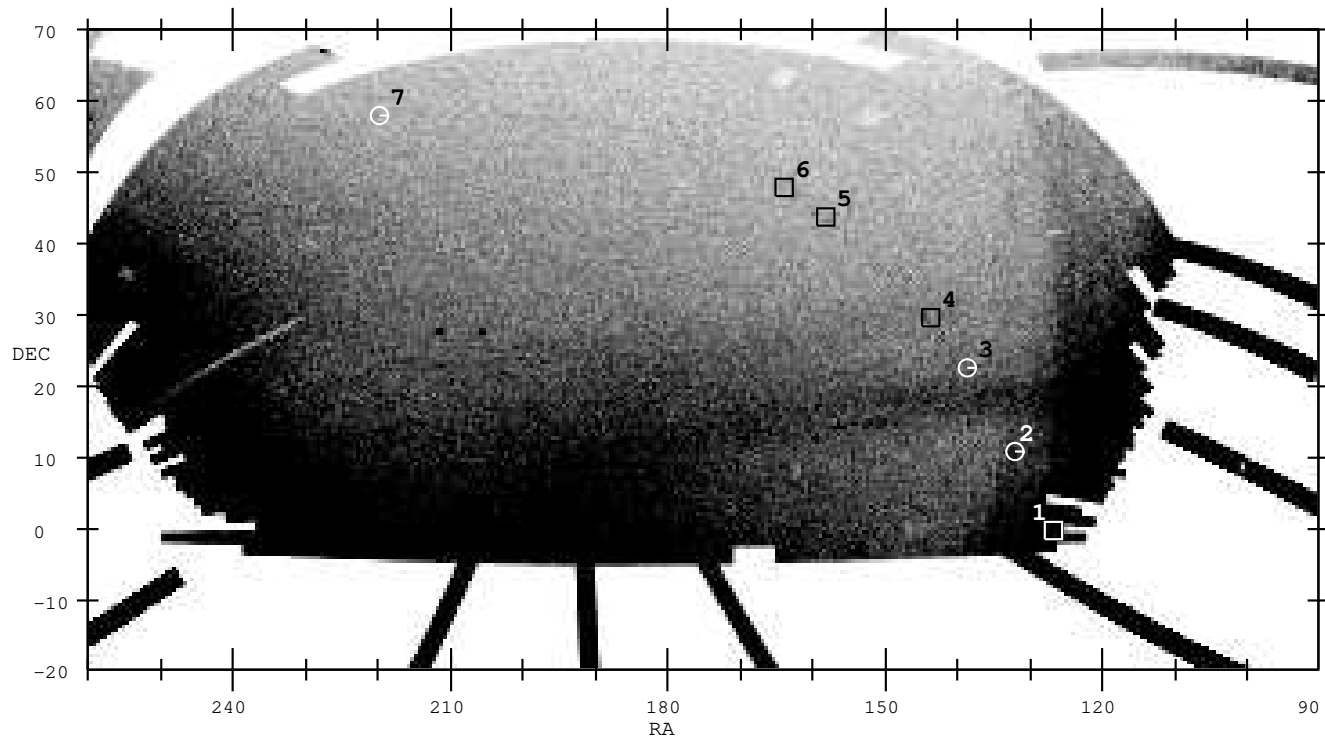
Table 3. Fixed Galactic Potential Parameter Values

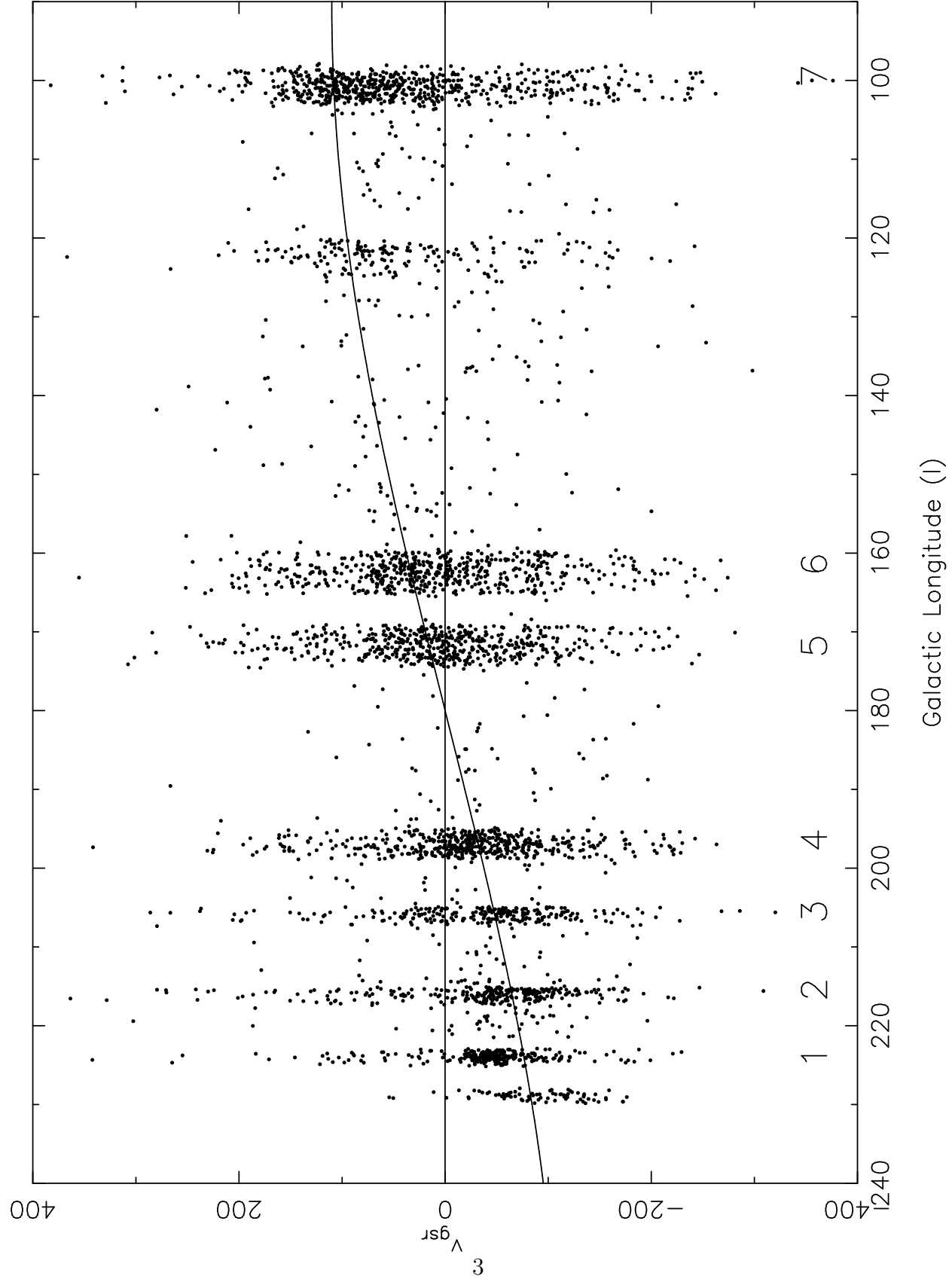
Parameter	Value
α	1.0
M_{disk}	$1.0 \times 10^{11} M_{\odot}$
M_{bulge}	$3.4 \times 10^{10} M_{\odot}$
a	6.5 kpc
b	0.26 kpc
c	0.7 kpc
v_{halo}	114 km/s
q	1.0
d	12 kpc

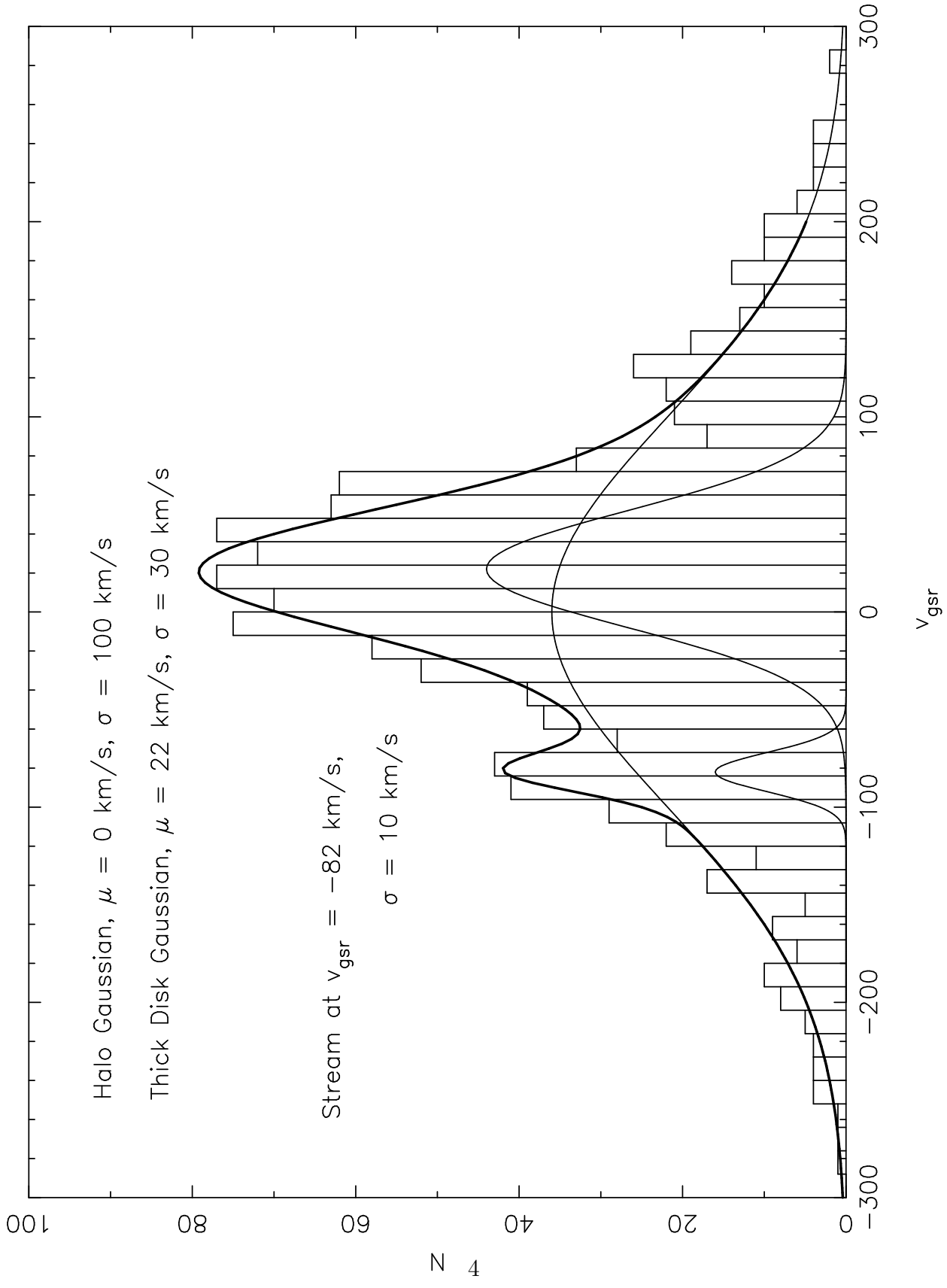
Table 4. Fit Parameters

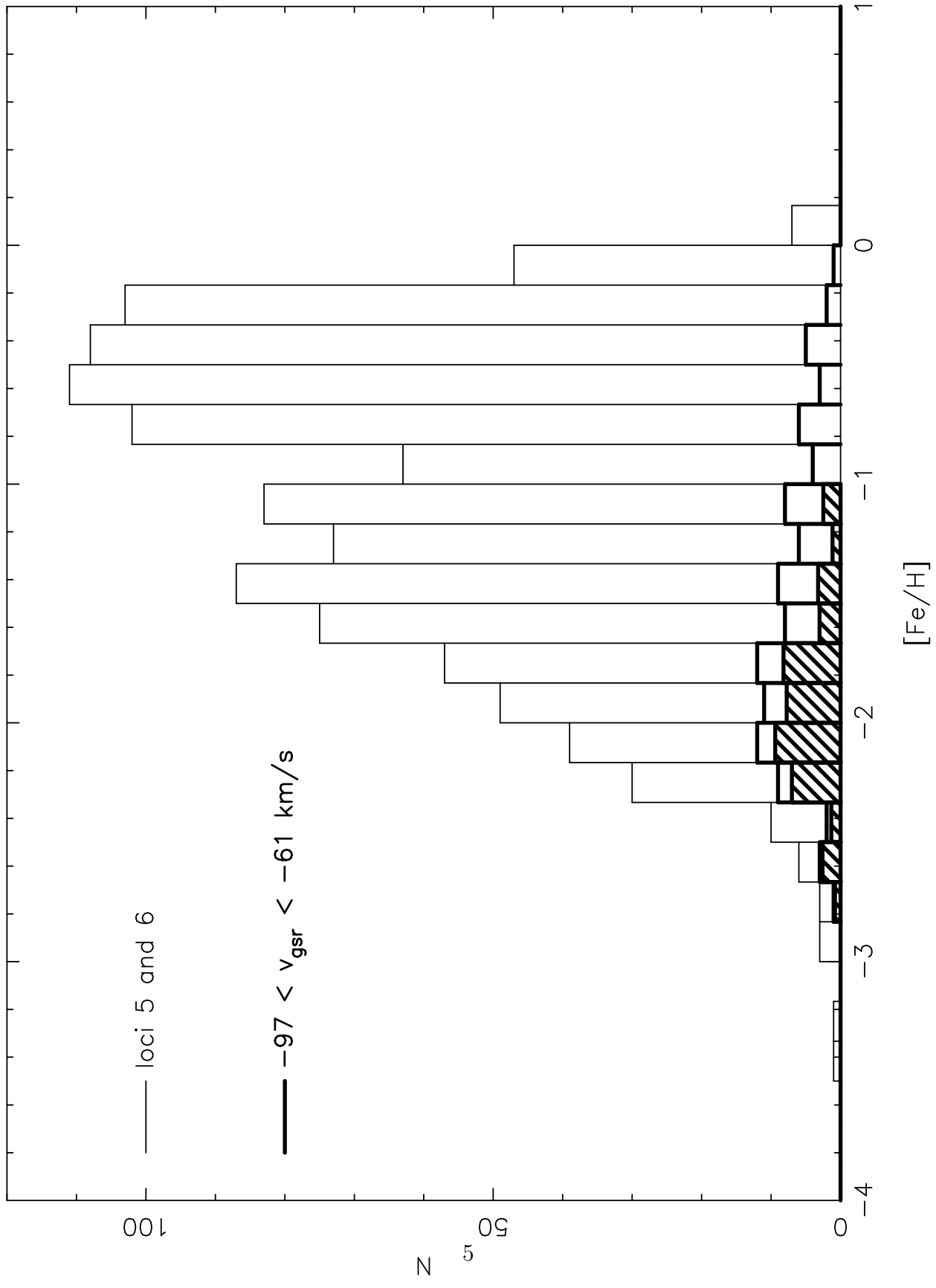
Fit Parameter	Description	Step Size	Random Selection Range
R_5	Sun-centered distance of Region 5	0.1 kpc	5 : 13 kpc
$v_{x,5}$	X Velocity of Region 5	1 km/s	-130 : -60 km/s
$v_{y,5}$	Y Velocity of Region 5	1 km/s	-320 : -230 km/s
$v_{z,5}$	Z Velocity of Region 5	1 km/s	-80 : -120 km/s

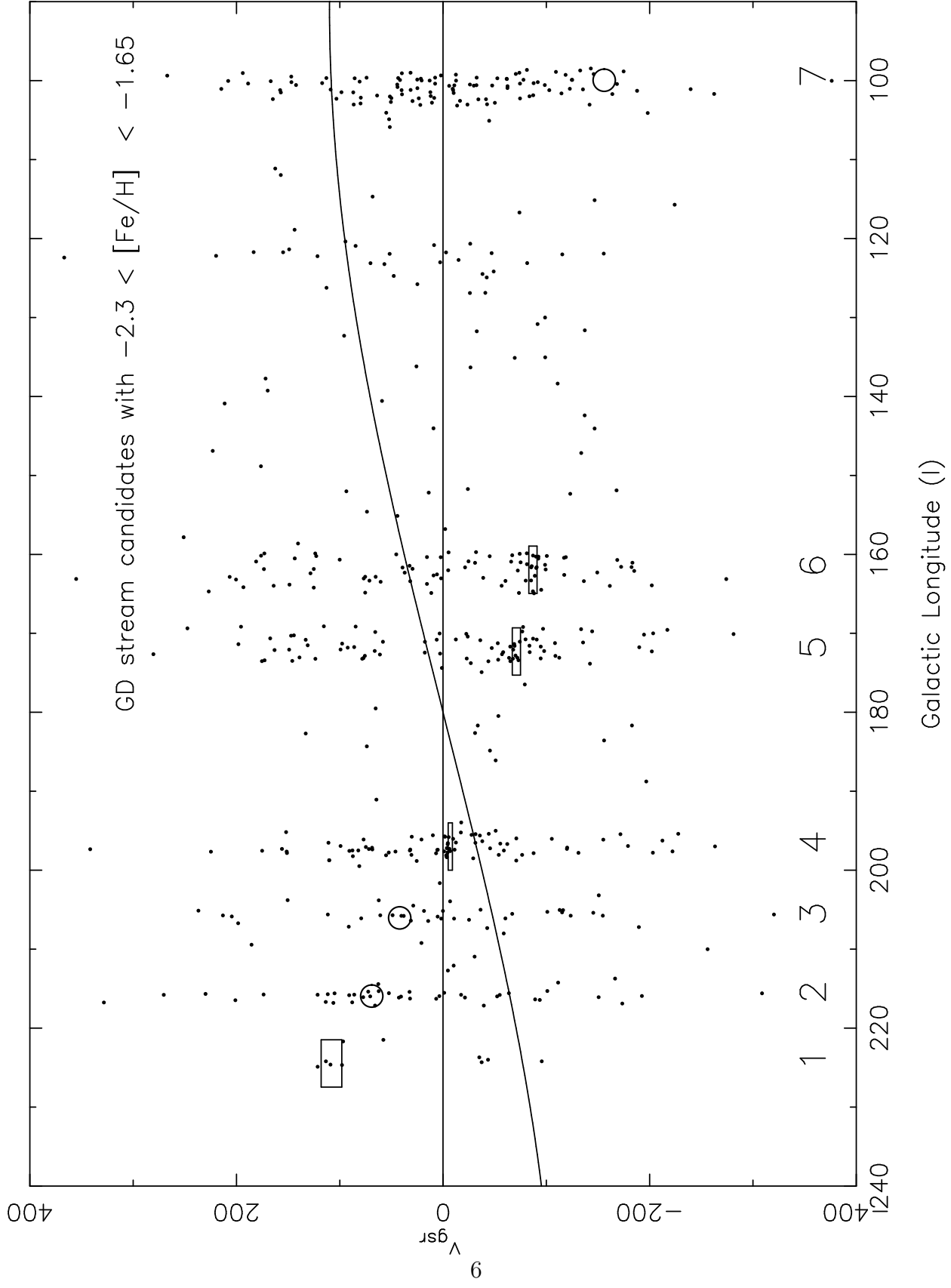


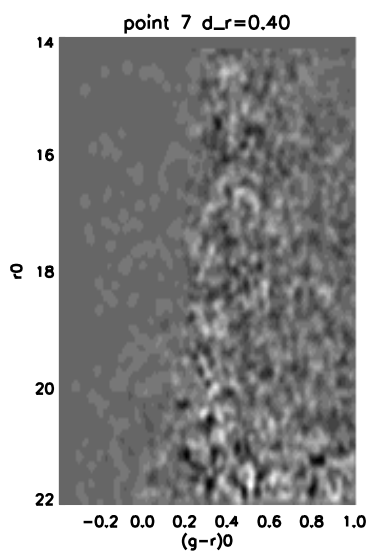
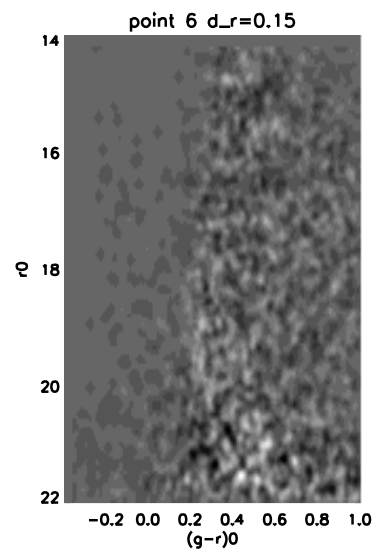
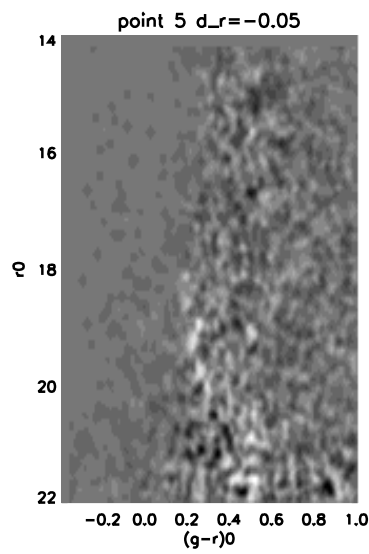
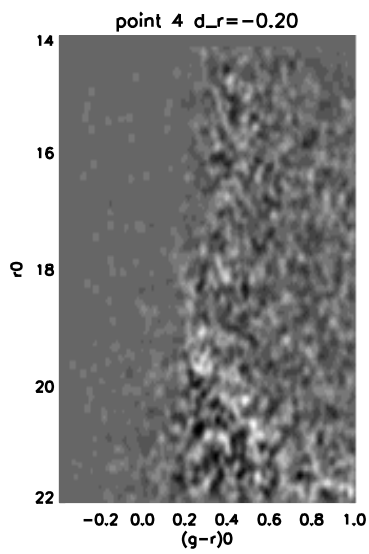
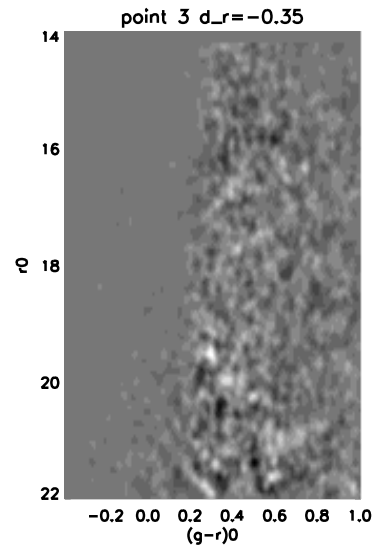
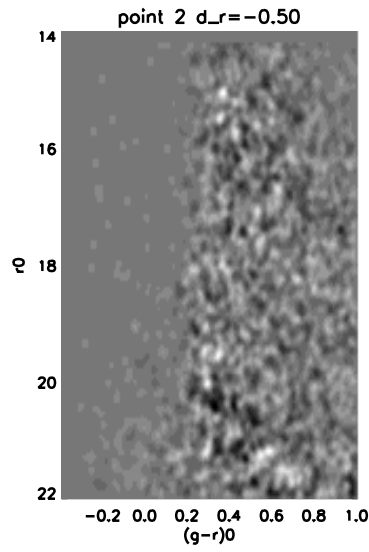
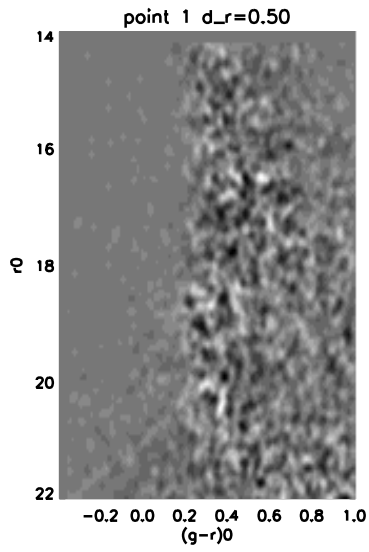


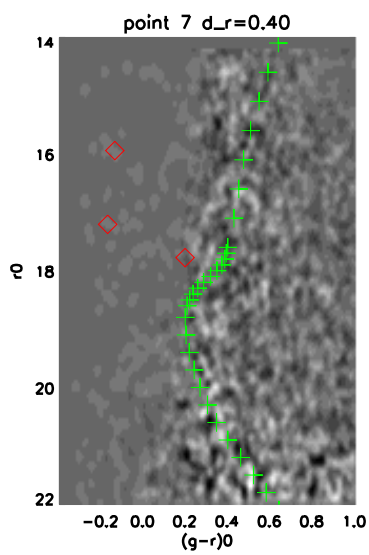
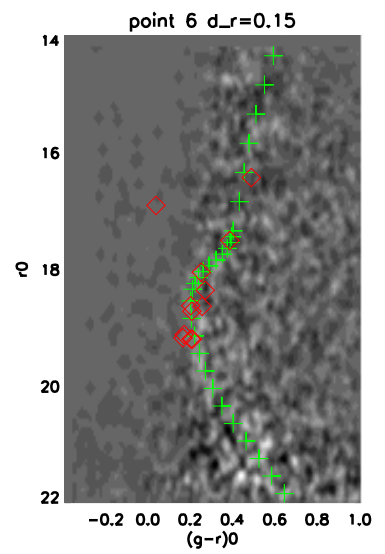
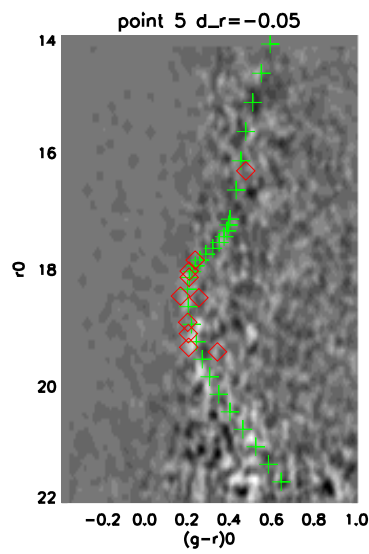
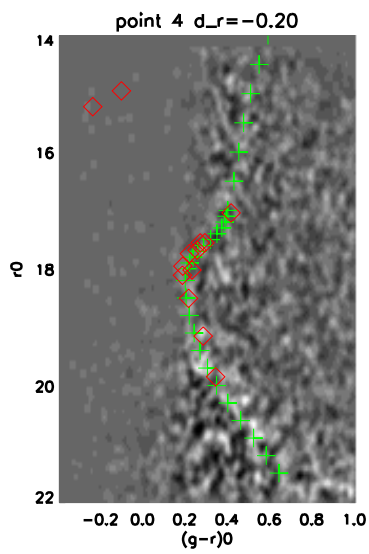
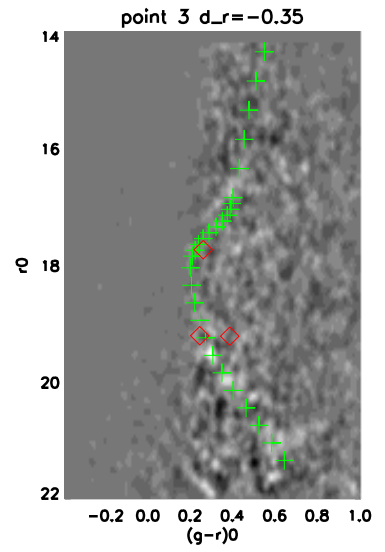
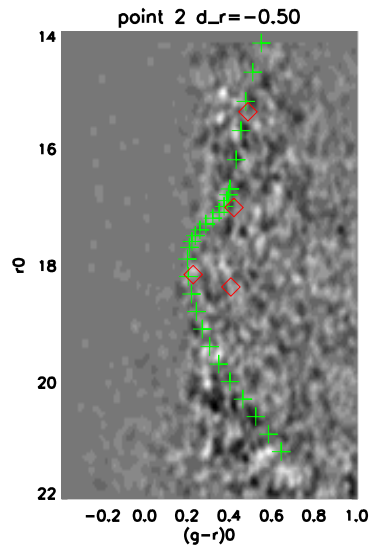
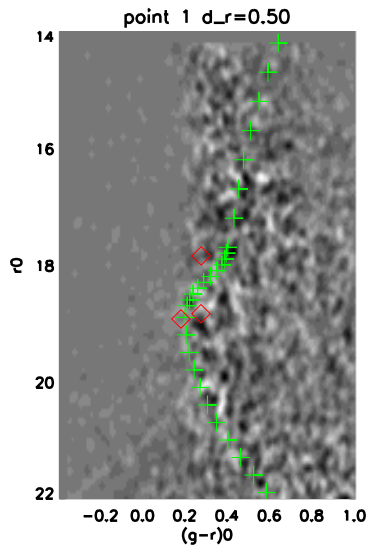


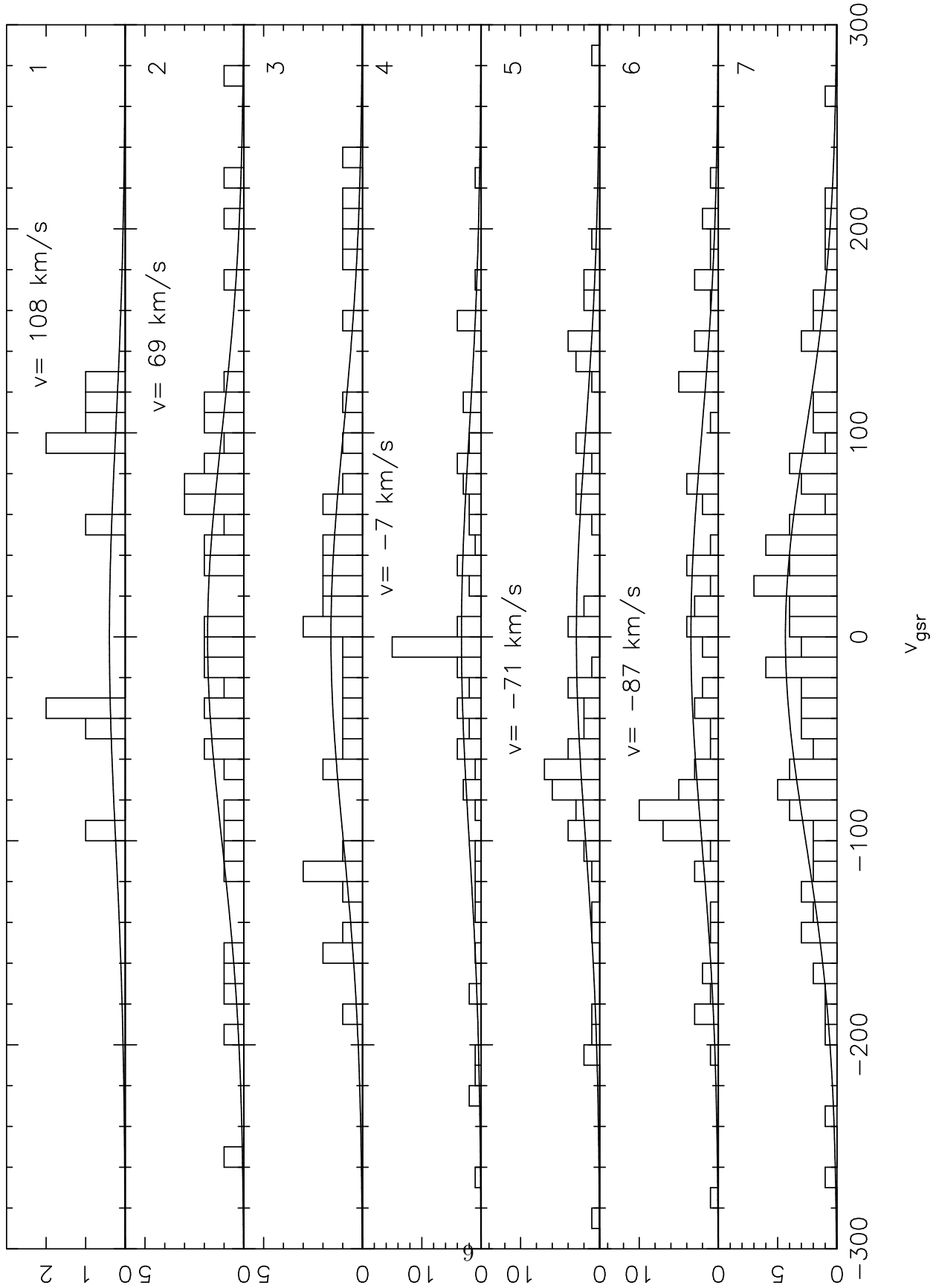


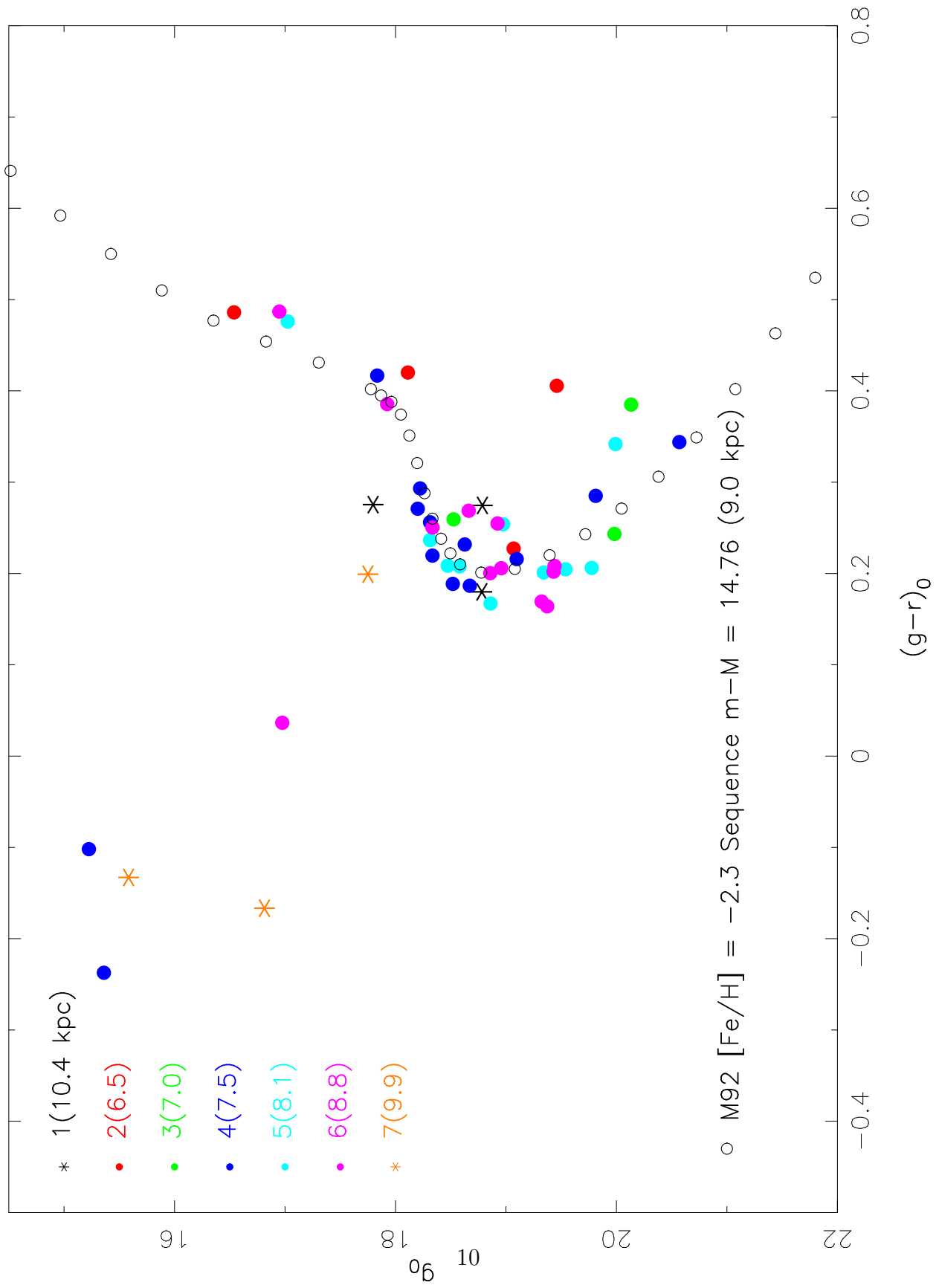


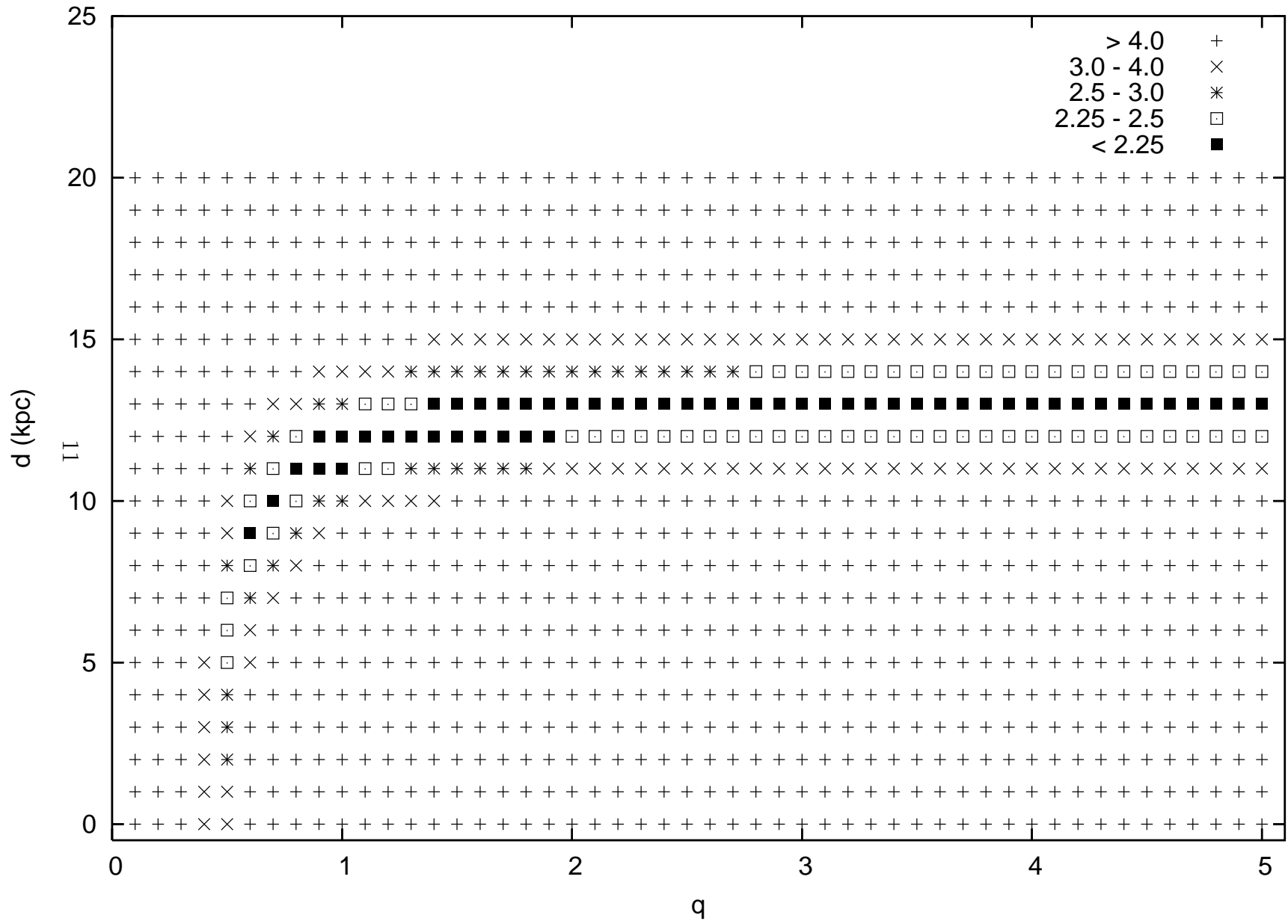












GD-1 Stream orbit
 (rectangular Galactic coordinates)

